

VICTORIA UNIVERSITY
MELBOURNE AUSTRALIA

Untargeted proteomics enables ultra-rapid variant prioritisation in mitochondrial and other rare diseases

This is the Published version of the following publication

Hock, Daniella H, Caruana, Nikeisha, Semcesen, Liana N, Lake, Nicole J, Formosa, Luke E, Amarasekera, Sumudu SC, Stait, Tegan, Tregoning, Simone, Frajman, Leah E, Bournazos, Adam M, Robinson, David RL, Ball, Megan, Reljic, Boris, Ryder, Bryony, Wallis, Mathew J, Vasudevan, Anand, Beck, Cara, Peters, Heidi, Lee, Joy, Tan, Natalie B, Freckmann, Mary-Louise, Harris, Madeleine, Martin, Ellenore M, McGrath, Pauline, Atthow, Catherine, Elbaum, Yoni, MacArthur, Daniel G, Balasubramaniam, Shanti, Siira, Stefan J, Simons, Cas, Salleveld, Suzanne CEH, Ghaoui, Roula, Davis, Ryan L, Murray, Sean, Coman, David, Stojanovski, Diana, Filipovska, Aleksandra, Karlaftis, Vasiliki, Attard, Chantal, Monagle, Paul, Samarasinghe, Amanda, Brown, Rosie, Bi, Weimin, Lek, Monkol, McFarland, Robert, Taylor, Robert, Ryan, Michael T, Cooper, Sandra T, Stark, Zornitza, Christodoulou, John, Compton, Alison G, Thorburn, David and Stroud, David A (2025) Untargeted proteomics enables ultra-rapid variant prioritisation in mitochondrial and other rare diseases. *Genome Medicine*, 17 (1). ISSN 1756-994X

The publisher's official version can be found at

<https://doi.org/10.1186/s13073-025-01467-z>

Note that access to this version may require subscription.

Downloaded from VU Research Repository <https://vuir.vu.edu.au/49643/>

RESEARCH

Open Access



Untargeted proteomics enables ultra-rapid variant prioritisation in mitochondrial and other rare diseases

Daniella H. Hock^{1,2,3*}, Nikeisha J. Caruana^{1,4}, Liana N. Semcesen¹, Nicole J. Lake⁵, Luke E. Formosa⁶, Sumudu S. C. Amarasekera², Tegan Stait², Simone Tregoning², Leah E. Frajman², Adam M. Bournazos^{7,8,9}, David R. L. Robinson¹, Megan Ball^{2,11,15}, Boris Reljic^{1,6}, Bryony Ryder¹², Mathew J. Wallis^{13,14}, Anand Vasudevan¹⁰, Cara Beck³, Heidi Peters^{11,15}, Joy Lee^{3,15}, Natalie B. Tan^{2,3,11}, Mary-Louise Freckmann¹⁶, MitoMDT Diagnostic Network for Genomics and Omics, Vasiliki Karlaftis^{2,11}, Chantal Attard^{2,11}, Paul Monagle^{2,11,17,18}, Amanda Samarasinghe², Rosie Brown^{2,3}, Weimin Bi^{19,20}, Monkol Lek⁵, Robert McFarland^{21,22}, Robert W. Taylor^{21,22}, Michael T. Ryan⁶, Sandra T. Cooper^{7,8,9}, Zornitza Stark^{2,3,11}, John Christodoulou^{2,3,11}, Alison G. Compton^{2,3,11}, David R. Thorburn^{2,3,11*} and David A. Stroud^{1,2,3*}

Abstract

Background Only half of individuals with suspected rare diseases receive a genetic diagnosis following genomic testing. A genetic diagnosis allows access to appropriate care, restores reproductive confidence and reduces the number of potentially unnecessary interventions. A major barrier is the lack of disease agnostic functional tests suitable for implementation in routine diagnostics that can provide evidence supporting pathogenicity of novel variants, especially those refractory to RNA sequencing.

Methods Focusing on mitochondrial disease, we describe an untargeted mass-spectrometry based proteomics pipeline that can quantify proteins encoded by > 50% of Mendelian disease genes and > 80% of known mitochondrial disease genes in clinically relevant sample types, including peripheral blood mononuclear cells (PBMCs). In total we profiled > 90 individuals including undiagnosed individuals suspected of mitochondrial disease and a supporting cohort of disease controls harbouring pathogenic variants in nuclear and mitochondrial genes. Proteomics data were benchmarked against pathology accredited respiratory chain enzymology to assess the performance of proteomics as a functional test. Proteomics testing was subsequently applied to individuals with suspected mitochondrial disease, including a critically ill infant with a view toward rapid interpretation of variants identified in ultra-rapid genome sequencing.

Results Proteomics testing provided evidence to support variant pathogenicity in 83% of individuals in a cohort with confirmed mitochondrial disease, outperforming clinical respiratory chain enzymology. Freely available

*Correspondence:

Daniella H. Hock
daniella.hock@unimelb.edu.au

David R. Thorburn
david.thorburn@mcri.edu.au

David A. Stroud
david.stroud@unimelb.edu.au

Full list of author information is available at the end of the article



© The Author(s) 2025. **Open Access** This article is licensed under a Creative Commons Attribution 4.0 International License, which permits use, sharing, adaptation, distribution and reproduction in any medium or format, as long as you give appropriate credit to the original author(s) and the source, provide a link to the Creative Commons licence, and indicate if changes were made. The images or other third party material in this article are included in the article's Creative Commons licence, unless indicated otherwise in a credit line to the material. If material is not included in the article's Creative Commons licence and your intended use is not permitted by statutory regulation or exceeds the permitted use, you will need to obtain permission directly from the copyright holder. To view a copy of this licence, visit <http://creativecommons.org/licenses/by/4.0/>.

bioinformatic tools and criteria developed for this study (<https://rdms.app/>) allow mitochondrial dysfunction to be identified in proteomics data with high confidence. Application of proteomics to undiagnosed individuals led to 6 additional diagnoses, including a mitochondrial phenocopy disorder, highlighting the disease agnostic nature of proteomics. Use of PBMCs as a sample type allowed rapid return of proteomics data supporting pathogenicity of novel variants identified through ultra-rapid genome sequencing in as little as 54 h.

Conclusions This study provides a framework to support the integration of a single untargeted proteomics test into routine diagnostic practice for the diagnosis of mitochondrial and potentially other rare genetic disorders in clinically actionable timelines, offering a paradigm shift for the functional validation of genetic variants.

Keywords Proteomics, Genetic diagnostics, Mendelian disease, Ultra-rapid genome sequencing, Variant prioritisation

Background

Despite advances in genomic sequencing approaches, only 35–70% of individuals with suspected rare disease receive a molecular diagnosis following whole exome sequencing (WES) or whole genome sequencing (WGS) [1–9]. Negative cases generally remain undiagnosed due to variants being refractory to short-read sequencing approaches or when variants of uncertain significance (VUS, class 3) are detected, requiring functional evidence to be upgraded to likely pathogenic (class 4) or pathogenic (class 5) [10].

Mitochondrial disease is an umbrella term for a group of over 300 rare monogenic disorders affecting mitochondrial energy production in the form of ATP [11]. These disorders can arise from sporadic or inherited variants in either nuclear or mitochondrial DNA (mtDNA), presenting at any stage of life with a myriad of symptoms affecting either a single organ or in a multisystemic manner [12]. Mitochondrial diseases affect approximately 1 in 5000 live births [13] with limited treatments available, reinforcing the importance of a genomic diagnosis for early intervention in affected individuals. A genomic diagnosis also facilitates informed reproductive options such as prenatal diagnosis (PND) and assisted reproductive technologies such as preimplantation genetic testing (PGT) and mitochondrial replacement therapy (MRT) [14].

Functional approaches to assess VUS pathogenicity in mitochondrial disease have historically relied on targeted and low throughput tests such as respiratory chain enzymology (RCE), SDS–polyacrylamide gel electrophoresis (PAGE) or blue native (BN)-PAGE and immunoblotting. RCE assesses the activity of the mitochondrial respiratory chain complexes I–IV and is typically normalised to the activity of a single enzyme, citrate synthase (CS), to account for variability in mitochondrial content determined by sample quality, amount and storage [15]. Western blotting has also been used for the confirmation of VUS pathogenicity based on protein abundance or differential size,

although it relies on having a strong genetic lead for disease causation from genomic data and the commercial availability of antibodies for the desired protein.

Other non-targeted functional approaches such as transcriptomics and proteomics have also been applied to the diagnosis of mitochondrial diseases. In selected cohorts, transcriptomics has been shown to increase the diagnosis of mitochondrial disorders by 10–16% [16, 17] and in other rare Mendelian disorders by 7–17% [18–20]. Although transcriptomic analysis can be a powerful tool in assessing pathogenicity of intronic and splice variants, this approach has limited power in offering functional information on missense variants, one of the most common and challenging classes of variants to assess [21, 22]. Splice variants are predicted to account for only 10% of pathogenic variants associated with autosomal recessive disorders [23], in line with current diagnostic rates achieved by transcriptomics. Missense variants, on the other hand, account for 60% of pathogenic variants [23] and approximately 40% of them are expected to result in reduced protein levels due to protein instability and turnover [24]. Proteomics can detect such changes and has been demonstrated to contribute to the diagnosis of Mendelian disorders by providing functional evidence for not only missense variants but also splice, deep intronic and copy number variants [16, 25–30]. Despite this, there is a lack of data to inform the general utility of proteomics in rare disease diagnoses as an untargeted approach like genomics and transcriptomics.

Here, we present a systematic analysis demonstrating the utility of proteomics in the detection of rare mitochondrial disorders and provide the first validated pipeline for ultra-rapid functional testing using peripheral blood mononuclear cells (PBMCs). Reference proteomics data and associated bioinformatics tools for performing the proteome analysis approaches developed for these investigations can be applied to user-uploaded data through our interactive web tool (<https://rdms.app/>).

Methods

Cohorts

Enrolment: Most participants were enrolled into one of a range of Institutional Review Board (IRB) approved study protocols based on the clinical presentation for suspected monogenic disease specific to each study listed under the Ethics approval and consent to participate section. VC13, VC15, VC24 and UDP5 were recruited through referral for clinical RCE testing through the Victorian Clinical Genetics Services (VCGS) of their skin fibroblasts (and on a secondary tissue, as indicated in Additional file 3: Table S2) with proteomics studies performed as an add-on test for method development. UDP1 was recruited and enrolled through the Mito Flagship project (HREC/16/MH/251) [31], a previous prospective genomics and multi-omics study, and consented to data sharing and publication. UDP4, SC3 and all fibroblast and skeletal muscle controls used in this study were recruited to an unpublished retrospective genomics and multi-omics study (HREC/RCH/34228) with a waiver of consent. UDP6, UDP7 and UDP8 were recruited through the MitoMDT project (HREC/82160/RCHM-2022), a prospective national genomics and multi-omics study with all participants consenting to data sharing and publication. The two skeletal muscle biopsies (SC1 and SC2) were referred through the NHS Highly Specialised Mitochondrial Laboratory (Newcastle upon Tyne Hospitals NHS Foundation Trust) for investigations of a likely mitochondrial genetic disease (REC 2002/205). The fibroblast sample (SC5) was previously published [26] and PBMCs (SC4) collected at the time were included in this study. All BMC controls were recruited into the HAPPI Kids study (HREC/RCH/34183) [32].

Sample collection, size and details: All fibroblast cell lines used in this study were derived from skin biopsy in clinically accredited tissue culture laboratories, skeletal muscle samples were derived from skeletal muscle biopsies and lymphoblastoid cell lines (LCLs) and peripheral blood mononuclear cells (PBMCs) derived from whole blood. For BMC samples, 36 were controls recruited and collected as part of the HAPPI Kids study as previously published [32], with the remainder collected as part of the MitoMDT study with the exception of SC4 which was collected from the same individual as the fibroblast sample (SC5) as previously published [26]. All published participants from the validation (VC) and supporting cohorts (SC) have a corresponding publication describing original study details, and clinical presentation and respiratory chain enzymology results (including on a secondary tissue, if performed) indicated in Additional file 1: Table S1. The 24 individuals in the VC were drawn from a range of Institutional Review Board (IRB) approved studies totalling more than 500 individuals with established

genetic diagnoses to represent different patterns of respiratory chain defects. Genetic sex was not reported as this study did not involve an analysis of sex differences.

Analyses: Quantitative proteomics was performed on all fibroblast samples from VC and all samples from the KC, UDP and SC. Clinical respiratory chain enzymology was performed on fibroblasts for all VC individuals, and skeletal muscle and lymphoblastoid cell lines for specific participants as indicated in Additional file 3: Table S2. cDNA studies or transcriptomic analysis were performed on UDP4, UDP7 and UDP8. For quantitative proteomic analysis, all fibroblast samples in the VC cohort were compared to the same set of 5 controls that were prepared and analysed within each batch. Skeletal muscle samples were compared to a set of 3 controls, while fibroblasts and PBMCs were compared to a set of 4–5 controls as indicated in the corresponding volcano plot. SC5 data were retrieved from a published source [26]. For UDP4 transcriptomics, 89 control muscle samples were used for outlier detection.

Genomic investigations

Genomic investigations resulting in diagnosis of patients within the validation cohort (VC) are described in the publications indicated by PMID within Additional file 1: Table S1, with the exceptions of VC13 (*SDHAF1*), VC15 (*UQCRC2*) and VC24 (*FARS2*) which are as follows: Individual VC13 (*SDHAF1*) underwent clinical singleton WES through Baylor Genetics as previously described [33]. For individual VC15 (*UQCRC2*), homozygosity mapping from Illumina HumanCytoSNP-12 v2.1 array data identified substantial long contiguous stretches of homozygosity (LCSH) accounting for ~3.7% of the genome. Due to the observed complex III RCE defect in this patient, candidate gene sequencing of exons using genomic DNA through PCR and Sanger sequencing was performed on complex III-related genes *UQCC1* and *UQCRC2*, which lay within these regions of LCSH (primers available upon request). Blood DNA for individual VC24 (*FARS2*) underwent clinical singleton WES testing through the Victorian Clinical Genetics Service (VCGS) as previously described [34]. Mitochondrial DNA sequencing (mtDNAseq) was also used to quantify mtDNA variant heteroplasmy levels for individuals VC6 (*MT-ND1*) and VC12 (*MT-ND5*) as previously described [34]. Individuals within the undiagnosed patient (UDP) cohort were investigated as follows: blood DNA from UDP1 (*MT-ATP6*) underwent WES with mtDNAseq as part of the Australian Genomics Mitochondrial Flagship as described [34]. For individual UDP4 (*CCDC47*), sequencing and analysis was performed as previously described [30]. Individual UDP5 (*NDUFA10*) had the Comprehensive Metabolism Panel performed by

Blueprint Genetics. Individuals UDP6 (*NDUFA13*) and UDP7 (*NDUFAF6*) both underwent clinical trio WES through the Victorian Clinical Genetics Service (VCGS) [34]. UDP8 (*NDUFS8*) had acute-care rapid trio WGS and analysis at the VCGS as previously published [7].

Respiratory chain enzymology

Respiratory chain enzyme activities in fibroblasts and skeletal muscle were measured by spectrophotometry as described [15]. Complex I (CI) was measured as rotenone-sensitive NADH:coenzyme Q₁ oxidoreductase, complex II (CII) as succinate:coenzyme Q₁ oxidoreductase, complex III (CIII) as decylbenzylquinol:cytochrome *c* reductase, and complex IV (CIV) as cytochrome *c* oxidase. Citrate synthase (CS) was measured as production of coenzyme A (CoA.SH) from oxaloacetate using the thiol reagent 5,5'-dithio-bis-(2-nitrobenzoic acid). Enzyme activities were calculated as initial rates (CI, CII and CS) or as first-order rate constants (CIII and CIV) [15].

Cell culture conditions

Fibroblast and HEK293T cell lines were cultured in Dulbecco's Modified Eagle Medium (DMEM) high glucose, sodium pyruvate and glutamine (Sigma-Aldrich) supplemented with 10% (v/v) foetal calf serum (FCS; CellSera), 100 U/ml penicillin–streptomycin (Gibco) and 50 µg/ml uridine. Cells were maintained at 37 °C with 5% CO₂.

Generation of knockout lines

The *NDUFS2*^{KO} cell line was generated using a CRISPR/Cas9 plasmid encoding the guide RNA 5'-TGAGGGCTTTGTGCGGCTTCCGG-3' cloned into the pSpCas9-2A-GFP vector [35]. The CRISPR was transfected into HEK293T cells and single cells were obtained by fluorescence-activated cell sorting at the Monash Flow Cytometry Platform (Flowcore). Single cell populations were screened by loss of cell viability on galactose-containing DMEM and subsequently validated by the loss of protein by western blotting and indel sequencing, which identified two deletions c.[18_36del] and c.[17_42del] (Additional file 1: Table S1). The *UQCRC2*^{KO} cell line was generated using a CRISPR/Cas9 plasmid encoding the guide RNA 5'-CACCGGTACTTACACATCACCCGC designed using the CHOPCHOP tool and sub-cloned into pSpCas9(BB)-2A-GFP vector as previously described [35]. The plasmids were validated by sequencing and then transfected into target cell lines using LipofectamineTM 3000 Transfection Reagent (Thermo Fisher Scientific) according to manufacturer's guidelines. Single cells expressing GFP were isolated on a FACS Aria Fusion (BD Biosciences) cell sorter and clonal populations were subsequently screened for relevant gene knockouts using

SDS-PAGE and immunoblotting and indel sequencing, which identified two deletions c.[9141_9199del] and [9146_9167del] (Additional file 1: Table S1). The *SURF1*^{KO} cell line was generated using a CRISPR/Cas9 system with the HEK293T parental cell line. Two guide RNAs targeting the 5'UTR and exon 2 regions of *SURF1* were cloned into individual pSpCas9-2A-GFP vectors (Addgene, plasmid 48138) [36]. Both constructs were transfected simultaneously into HEK293T cells using Lipofectamine 3000 (Thermo Fisher Scientific), according to the manufacturer's instructions. Verification of successful HEK293T *SURF1*^{KO} was performed via three primer screening PCR to amplify incorporated indels and by SDS-PAGE immunoblotting. The product of external primers (outside the double CRISPR target sites) underwent M13 primer Sanger sequencing of alleles, using the TopoTM TA Cloning Kit (Thermo Fisher Scientific) as per the manufacturer's instructions. Sequencing identified two deletions [c.18_219del] and [c.18_221delinCG] (Additional file 1: Table S1). The *ATP5PD*^{KO} cell line was generated using a CRISPR/Cas9 plasmid encoding the guide RNA 5'-CACCGCCTTTCCTTGTTGGGCA GGT designed using the CHOPCHOP tool and sub-cloned into pSpCas9(BB)-2A-GFP vector as previously described [35]. The plasmids were validated by sequencing and then transfected into target cell lines using LipofectamineTM 3000 Transfection Reagent (Thermo Fisher Scientific) according to manufacturer's guidelines. Single cells expressing GFP were isolated on a Fluorescence-Activated Cell Sorting Aria Fusion (BD Biosciences) cell sorter and clonal populations were subsequently screened for relevant gene knockouts using indel sequencing, which identified a single deletion c.[33481insT] (Additional file 1: Table S1).

PBMC isolation from whole blood

Neonatal blood samples were collected from healthy neonates following routine intramuscular administration of vitamin K. For older infants and children ages 30 days to 18 years, venous blood samples were obtained from hospital outpatients undergoing minor elective day surgery. An outline of the study protocol and complete detail of participant recruitment, inclusion and exclusion criteria and sample collection are described in our previously published HAPPI Kids study protocol [32]. PBMCs were isolated from fresh blood samples of the 36 HAPPI Kids controls using Ficoll[®]-Paque Plus (GE Healthcare Life Sciences) according to the instructions of the manufacturer with manual removal of the PBMC layer using a Pasteur pipette. For the UDP6 (*NDUFA13*), UDP7 (*NDUFAF6*) and UDP8 (*NDUFS8*) probands, PBMC isolation using Ficoll[®]-Paque Plus was performed in SepMateTM tubes (STEMCELL Technologies), based on

manufacturer's protocols with moderate braking applied for both washes, and a reduction in centrifugation speed and duration to 200 g for 5 min for the second wash.

Data-independent acquisition mass spectrometry of fibroblast, HEK293T and PBMCs cohorts and data analysis

Spectral library sample preparation

A HEK293T spectral library was generated from both whole cell and mitochondrial HEK293T samples to search data-independent acquisition (DIA) HEK293T knockout cell lines. A total of 100 µg of mitochondrial sample isolated from wild-type HEK293T cells underwent carbonate extraction at pH 11.5 to separate soluble and integral mitochondrial proteins, as previously described [37]. The resulting pellet and supernatant samples, as well as 25 µg whole cell HEK293T sample, were solubilised in lysis buffer for a final composition of 5% SDS and 50 mM triethylammonium bicarbonate (TEAB) pH 8.5. The lysed whole cell, mitochondrial pellet and supernatant samples were processed using S-trap™ Micro Spin Columns (ProtiFi) according to the manufacturer's instructions, where samples were reduced with 40 mM 2-chloroacetamide (CAA, Sigma) and alkylated with 10 mM tris(2-carboxyethyl)phosphine hydrochloride (TCEP; BondBreaker, Thermo Fisher Scientific). Isolated proteins were digested at 1:25 trypsin to protein ratio at 37 °C overnight and eluted peptides were dried down using a CentriVap Benchtop Vacuum Concentrator (Labconco). Fibroblasts and PBMCs spectral libraries were generated from whole cell samples of either five healthy fibroblast controls or PBMC pellets isolated from 39 healthy individuals ranging from 0 to 17 years old. Fibroblast or PBMC pellets were solubilised 5% SDS and 50 mM TEAB pH 8.5, and total protein determined by Pierce bicinchoninic acid (BCA) Protein Assay Kit (Thermo Fisher Scientific). A total of 25 µg for each control was processed using the S-Trap™ Micro Spin Columns (ProtiFi), as described above.

Peptides from HEK293T, fibroblast and PBMC samples were reconstituted in 0.5% formic acid (FA) for fractionation. Fibroblast and PBMC control samples were pooled upon reconstitution to create a single fibroblast, HEK293T and PBMC peptide mixture and loaded onto a strong cation exchange (Empore Cation Exchange-SR, Supelco Analytical) stage tips made as described [38]. Stage tips were washed with 20% acetonitrile (ACN) and 0.5% FA and eluted over seven fractions of increasing concentrations of ammonium acetate (45–300 mM), 20% ACN and 0.5% FA for whole cell fibroblasts, PBMC and HEK293T samples. HEK293T mitochondrial and supernatant samples were collected over five fractions. All samples underwent a final elution with 5%

ammonium hydroxide and 80% ACN, followed by concentration using a CentriVap Benchtop Vacuum Concentrator (Labconco). Fractions were desalted on SDB-XC (poly(styrene-divinyl-benzene); Supelco Analytical) stage tips made in-house as previously described [38].

Spectral library mass spectrometry data-dependent acquisition

Fractions were reconstituted in 0.1% trifluoroacetic acid (TFA) and 2% ACN and each library was analysed by liquid chromatography (LC)-tandem mass spectrometry (MS/MS) on an Orbitrap Eclipse Mass Spectrometer (Thermo Fisher Scientific) operating on DDA mode over a 125-min gradient. Tryptic peptides were loaded onto an Acclaim Pepmap nano-trap column (Dinoex-C18, 100 Å, 75 µm×2 cm) at an isocratic flow of 5 µl/min of 2% ACN and 0.1% FA for 6 min before switching with an Acclaim Pepmap RSLC analytical column (Dinoex-C18, 100 Å, 75 µm×50 cm). The separation of peptides was performed using a nonlinear 125-min gradient of solvent A (5% dimethyl sulphoxide (DMSO), 0.1% FA) and solvent B (5% DMSO, 100% ACN, 0.1% FA). The flow gradient was (i) 0–6 min at 3% solvent B, (ii) 6–95 min at 3–23% solvent B, (iii) 95–105 min at 23–40% solvent B, (iv) 105–110 min at 40–80% solvent B, (v) 110–115 min at 80–80% solvent B, (vi) 115–116 min at 80–3% solvent B and equilibrated at 3% solvent B for 10 min before the next injection. Briefly, data were collected using positive polarity with a MS1 scan range of 375–1500 m/z and resolution set to 120,000. Other MS1 instrument parameters include ACG target of 4e5, maximum injection time of 50 ms and isolation window of 1.6. MS2 instrument parameters include scan range of 150–2000 m/z, resolution of 15,000, HCD collision energy of 30%, ACG target of 5e3, maximum injection time of 22 ns and dynamic exclusion of 30 s.

Sample preparation of HEK293T, PBMC and fibroblast cell lines

Whole cell pellets of HEK293T cells, PBMCs and fibroblasts were collected and washed twice with PBS before resuspension in 5% SDS, 50 mM tetraethylammonium bromide (TEAB) pH 8.5 buffer and 125 U of benzonase per ml (Sigma-Aldrich). Skeletal muscle samples were solubilised with a probe sonicator with 30% amplitude in 5% SDS, 50 mM TEAB pH 8.5 buffer on ice with a cycle of 10 s on 10 s off for 1 min and clarified at 16,000×g for 5 min. Protein concentration was performed with Pierce BCA Protein Assay Kit (Thermo Fisher Scientific) and 25 µg of each sample was aliquoted in triplicates for patients and singlicate for individual controls (N=3–5). Samples were processed using S-trap™ micro spin columns (ProtiFi) according to the manufacturer's

instructions. Proteins were digested with trypsin (Thermo Fisher Scientific) at 1:10 trypsin to protein ratio. Peptides were dried down using a CentriVap Benchtop Vacuum Concentrator (Labconco).

Mass spectrometry data-independent acquisition

Peptides were reconstituted in 45 µl of 2% ACN and 0.1% TFA and 2 µl was injected into an Orbitrap Eclipse mass spectrometer (Thermo Fisher Scientific) for LC-MS/MS analysis equipped with trap and analytical columns described above. All samples were analysed with the mass spectrometer operating in DIA mode for 125 min (HEK293T) or 95 min (fibroblasts, skeletal muscle, PBMCs). The separation of peptides was performed using a nonlinear gradient of solvent A and solvent B across 125 min for HEK293T knockout cell lines and 95 min for all other sample types (fibroblasts, PBMCs and skeletal muscle). Briefly, for the 125-min method, the flow gradient was (i) 0–6 min at 3% solvent B, (ii) 6–95 min at 3–23% solvent B, (iii) 95–105 min at 23–40% solvent B, (iv) 105–110 min at 40–80% solvent B, (v) 110–115 min at 80–80% solvent B, (vi) 115–116 min at 80–3% solvent B and equilibrated at 3% solvent B for 10 min before the next injection. The data were collected using positive polarity with a MS1 scan range of 350–1200 m/z at a resolution of 120,000. Other MS1 instrument parameters include ACG target of 1e6, maximum injection time of 50 ms and isolation window of 24 with 1 m/z overlap. For MS2 parameters, the scan range was 200–2000 m/z at 15,000 resolution, HCD collision energy of 30%, AGC target of 1e6 and maximum injection time of 22 ms. For the 95-min method, the flow gradient was (i) 0–6 min at 3% solvent B, (ii) 6–7 min at 3–4% solvent B, (iii) 7–82 min at 4–25% solvent B, (iv) 82–86 min at 25–40% solvent B, (v) 86–87 min at 40–80% solvent B, (vi) 87–90 min at 80–80% solvent B, (vii) 90–91 min at 80–3% solvent B and equilibrated at 3% solvent B for 5 min before the next injection. Instrument parameters were consistent with those used in the 125-min method described above, with changes made to the following parameters: MS1 scan range of 350–1400 m/z, MS1 maximum injection time of 45 ms, isolation window of 13.7 and MS2 ACG target of 5e5.

Proteomic data search

For the spectral library, raw files were imported into Spectronaut® [39] (v.15.2.210819.50606 for HEK293T library, v.14.8.201029.4778 for fibroblasts library, v.16.0.220606.53000 for PBMCs library) and the three libraries were generated using the ‘Pulsar’ option with default BGS Factory settings, searching against Uniprot human database containing reviewed canonical and isoforms sequences (42,386 entries). The resulting HEK293T

library contained 194,270 precursors, the fibroblast library contained 131,627 precursors, and the PBMC library contained 148,522 precursors. For DIA samples, raw files were imported into Spectronaut® and searched against the libraries generated above. Default BGS Factory search parameters were used with changes made to exclude single hit proteins, no selection of ‘Major Group Top N’ and ‘Minor Group Top N’ and data filtering setting set to ‘Q-value’ or ‘Q-value sparse’ with ‘run-wise imputation’ as an imputing strategy. ‘Q-value’ datasets (unimputed) were used for generation of RCA values while ‘Q-value sparse’ with ‘run-wise imputation’ datasets were used to generate heatmaps and correlation plots to reduce missing values for visualisation, and in volcano plots for validation cohort (VC) and HEK293T knockout cohort (KC) cohorts or when the protein of interest was not well detected. UDP1 (*MT-ATP6*) data were also searched using the Spectronaut® BGS Factory direct DIA (library free) pipeline with the same above ‘Q-value’ settings (unimputed) and with the inclusion of an additional protein FASTA file containing the p.Thr228Met ATAD3A variant in the database search. SC1 and SC2 (*TMEM70*) skeletal muscle were searched with default BGS Factory direct DIA settings with changes as above.

Protein filtering and clean up

Proteins were filtered in each cohort to ensure that the data were of high quality and with a minimal amount of missing data for analysis. Proteins within the VC were filtered out if identified by a single peptide in all controls or proband samples, maintaining proteins that were identified by >2 peptides in both groups. Proteins were then filtered to least three or more valid values for the controls and at least two or more valid values for the proband samples. For the KC, proteins were filtered out if identified by a single peptide in all controls and proband samples. Proteins were then filtered to at least two valid values for the controls and at least two valid values for the knockout samples. For the undiagnosed proband cohort (UDP), proteins were filtered out if identified by a single peptide in all controls or proband samples. Proteins were then filtered for 70% valid values for the controls due to the different number of controls per batch and 70% valid values for the proband samples. For the supporting cohort (SC), samples SC1, SC2, SC3 and SC5 proteins were filtered out if identified by a single peptide in all controls or proband samples. Proteins were then filtered for 70% valid values for the controls and 70% valid values for the proband samples. Sample SC4 had no filtering completed as this was a previously published dataset [26] and the data were unlogged and complex subunit gene names manually updated to match the current MitoCarta3.0 [40] naming convention for complex

V subunits. For the 36 PBMC control samples (SC6-41), proteins were filtered out if they were identified by a single peptide across all 36 samples and further filtered for at least 70% valid values.

Relative complex abundance plots

Relative complex abundance (RCA) plots were generated for all VC, KC, SC and UDP cohorts and plots can be viewed within the RDMS Explorer platform (<https://rdms.app/>). All samples underwent a mitochondrial correction step where the mean of the mitochondrial proteins for each specific sample was determined using the average of all control mitochondrial proteins or proband mitochondrial proteins and then used as a mitochondrial correction factor for each group and applied to each sample. To develop the RCA plots, the average of the proband and controls was determined and then transformed to log10. The difference between the log10 of the proband and controls was determined and then unlogged. Statistical difference between the control and proband complex subunits was determined using an unpaired two-sided *t*-test and summary statistics including mean and the error bars indicating standard deviation were determined for each complex and the graph plotted within R (v.4.3.2). Complex subunits were determined using curated annotations from MitoCarta3.0 [40]. For Additional file 2: Fig. S3A, relative mitochondrial abundance from MitoCarta3.0 '+' entries were generated as above without the mitochondrial correction step. For Additional file 2: Fig. S3B, control mitochondrial abundance plots were generated using log2 abundances from MitoCarta3.0 '+' entries for each batch and significance performed with an ANOVA test.

Protein range graphs

Protein range graphs were developed using an in-house R script. The median of the protein of interest in control samples is calculated as well as the median of the proband replicates. The log2 fold-change is calculated between the proband and control and converted to percentage for the proband as the abundance relative to the control median for plotting. The range of the controls is also displayed as the abundance relative to the control median. The log2 abundance per standard deviation (SD) is rounded to one decimal place with the top axis SD present to determine how many standard deviations the protein is from the control median.

Volcano and correlation plots

The peptide and valid value cleaned matrices for all samples were annotated with MitoCarta3.0 [40] entries in Perseus [41]. All analyses were performed in Perseus v 1.6.14.0. Volcano plots were visualised using scatter

plot function from an unpaired two-sided using *p* value threshold of 0.05 in Perseus. For the correlation plots (Fig. 3B, Additional file 2: Fig. S2B), proteomic data searched with *q* value sparse with run-wise imputation settings were correlated via gene name using gene name entries and the logFCs in R and plotted using scatter plot function in Perseus. For Fig. 4C, previously published data from *MRPL50* fibroblasts [26] were correlated with *MRPL50* PBMCs using gene name entries and the logFCs in R and plotted using scatter plot function in Perseus.

Heatmaps and Venn diagrams

For heatmaps output matrices searched with *q* value sparse run-wise imputation settings Spectronaut runs were log₂ transformed and an unpaired two-sided *t*-test using *p* value for truncation was performed in Perseus for each cell line against their respective batch controls. The Morpheus software was used for heatmap visualisation (<https://software.broadinstitute.org/morpheus>) [42]. For Additional file 2: Fig. S1A, proteins were manually annotated based on MitoCarta3.0 as 'assembly factor' or 'complex I-V' and subset for visualisation in Morpheus using the following parameters metric 'one minus Pearson correlation', linkage method 'average', cluster 'rows' and group columns by 'complex/assembly factor'. *p* value results from the unpaired two-sided *t*-test statistical analysis were used to visualise the significance of each data point by overlaying the *p* value matrix onto the *t*-test matrix in Morpheus and using the option size by 'p-value matrix' size minimum '0' and maximum '1.301' (*p* value < 0.05). For the correlation heatmap plot (Additional file 2: Fig. S2A), hierarchical clustering was used with the following parameters in Morpheus: metric 'one minus Pearson correlation', linkage method 'average' and cluster 'columns'. Topographical heatmaps (Additional file 2: Fig. S1B) were generated from log₂-transformed fold-change from *t*-test in Pymol using the PDB structures (CI: 5LDW, CII: 1ZOY, CIII: 1BGY, CIV: 5Z62, CV: 7AJD) as previously described [35]. Venn diagrams were generated with DeepVenn (<https://www.deepvenn.com/>) [43] using gene names. Green (diagnostic-grade) and amber (borderline diagnostic-grade) lists for mitochondrial disease (v.0.787) and Mendeliome gene lists (v.0.12869) were retrieved from PanelApp Australia (<https://panelapp-aus.org/>) [44].

Principal component analysis and donut plots

PCA plots were generated in Perseus v 1.6.14.0 from the *t*-test fold-change data for VC cohort (Fig. 1B) or protein

abundances for PBMCs controls (Fig. 4B). Donut plots were generated in GraphPad Prism (v.10.2.0).

RNA sequencing and transcriptomic analysis

RNA sequencing and analysis was performed as described [25]. In brief, RNA was extracted from muscle using miRNeasy Mini Kit (Qiagen) and treated with RNase-Free DNase (Qiagen) and RNA quality and quantity measured using TapeStation RNA ScreenTape analysis (Agilent) and Qubit RNA HS (Thermo Fisher Scientific). UDP4 underwent RNAseq within a group of 10 undiagnosed patients with available muscle samples, all with an RNA integrity number of 7.2–8.9. The Kapa Biosystems mRNA Hyper Prep Kit was used to generate sequencing libraries from 500 ng RNA, and paired-end sequencing on an Illumina instrument was performed at the Yale Center of Genome Analysis to achieve 50–100 million read coverage.

For outlier detection, 100 control muscle samples were retrieved from GTEx using the Sequence Read Archive (SRA) toolkit and converted into FASTQ using Fastq-dump. Patient and control FASTQ files were aligned to hg38 human reference genome with GENCODE v26 annotations using STAR (v2.5.3a), with twopassMode='Basic' to enable detection of novel splice junctions, and duplicates marked using Picard (v2.9). RNA-SeQC (v2.3.4) was used to generate quality metrics from STAR-aligned bam files. Outliers were removed per the following criteria: (a) <45 million QC-passed reads, (b) <18,000 genes detected and (c) manual identification via principal component analysis. This resulted in the removal of 11 samples, leaving 89 control samples from muscle. Outlier expression was assessed using the DROP (Detection of RNA Outliers Pipeline) pipeline v0.9.0 (<https://github.com/gagneurlab/drop>), with default settings [45]. Analysis was restricted to 6106 genes, which included Mendeliome and 'MitoExome' genes, as described previously [25].

cDNA studies

When parental samples were unavailable for variant phasing or where cDNA splicing or stability studies were required (as for VC24-*FARS2*), cultured skin-derived fibroblasts were grown with or without cycloheximide (100 ng/ml for 24 h) before harvesting for RNA extraction, cDNA synthesis, PCR and cloning as previously described [46]. Total RNA extracted from skeletal muscle (UDP4-*CCDC47*) or fibroblasts (UDP7-*NDUFAF6*) for RNA sequencing was also synthesised into cDNA using the SuperScript III First-Strand Synthesis System (Thermo Fisher Scientific) as per both manufacturer's protocols and as described previously [46]. To examine mRNA splicing in *CCDC47*, PCR primers (5' GCGTGA

CTGAGCTACGGTT 3'; 5' CTCTGGGATGGCTTT ACATGG 3') were designed to amplify the entire ORF from cDNA. For UDP7 (*NDUFAF6*), the PCR primers (5' CTGGGGCACTGACCACTACT 3'; 5' CATGGGAAG GAACACCTTTCT 3') were used to amplify exons 1 to 6 from *NDUFAF6* cDNA. PCR products were analysed on 1% agarose (Bioline) gels using a 1-kb Plus DNA Ladder (Thermo Fisher Scientific) prior to cloning into a pCR2.1-TOPO vector using the TOPO TA cloning kit (Thermo Fisher Scientific) and transformation into TOP10 competent cells (Thermo Fisher Scientific). Individual colonies were examined and then underwent Sanger sequencing. For UDP8 (*NDUFS8*), 2.5 ml of whole blood was collected in a PAXgene Blood RNA Tubes and RNA was isolated using the PAXgene® blood RNA kit according to kit instructions. qScript Ultra first-strand synthesis system was used to make cDNA from 500 ng of RNA according to kit instructions. PCR was performed using forward primers in exons 1 and 6 and reverse primers in exon 7 (exon 1 forward 5' CGATTGACTGGCCTGCTTG 3'; exon 6 forward 5' ACCCGCTATGACATCGACAT 3'; exon 7 reverse 5' CACTTGTCCTCCGTTGTTGAG 3'). Pooled amplicons were barcoded and sequenced on a Nanopore PromethION flow cell. All demultiplexed samples were aligned to GRCh38 using minimap2 -ax splice -ub -k14 and single gene *NDUFS8* GRCh38 sequence using minimap2 -ax splice:hq -ub -k14 [47].

Results

To validate our untargeted proteomic approach in the detection of mitochondrial disorders, we first analysed primary fibroblast cell lines from a cohort of 24 patients with confirmed genetic diagnoses based on known pathogenic or likely pathogenic nuclear or mtDNA-encoded variants. This validation cohort (VC) included cell lines with defects in subunits or assembly factors for each of the five individual OXPHOS complexes as well as defects of mtDNA translation that impact multiple complexes, causing a combined OXPHOS biochemical defect (Fig. 1A, Additional file 1: Table S1). Principal component analysis showed that proteomes segregate according to their primary defect (Fig. 1B) and hierarchical clustering of OXPHOS subunits and assembly factors identified clear profiles (Additional file 2: Fig. S1A and B). We have previously shown similar profiles to be present in gene-edited HEK293T knockout lines of complex I subunits [35]. Comparison of mitochondrial proteomes from our validation cohort of fibroblast cell lines and corresponding gene-edited HEK293T knockout cell lines (knockout cohort, KC) showed good correlation of dysregulated proteins (Additional file 2: Figs. S2A and S1B).

The maximum theoretical coverage of known mitochondrial disease gene products from the fractionated

library was 80%, with a routine coverage of 64% in a standard 95-min library-supported DIA run from fibroblast samples (Fig. 1C). Our approach could also detect proteins corresponding to 37% of the Mendeliome (i.e. encoded by known disease genes) in a standard 95-min run, supporting the potential utility of proteomics as a disease agnostic test in the resolution of many rare monogenic disorders. In terms of variant type in the validation cohort, the most common type was nuclear coding single nucleotide variants (47%) followed by indel/deletion (19%), mtDNA single nucleotide variants (16%), splice site (13%) and deep intronic (6%) (Fig. 1D). We quantified the abundance of the protein of interest in 67% of our investigations with the most common outcome being the protein abundance readily quantified in controls and absent in proband (42%) followed by a decrease in the patient relative to controls (21%) (Fig. 1E). In 29% of cases the protein of interest was not detected in either proband or control fibroblasts. For the cases where the protein was identified in both proband and control fibroblasts, analysis of the standard deviation show that ND1 abundance in VC6 (*MT-ND1*) was 97% relative to control median and within the control distribution, while ND5 abundance in VC12 (*MT-ND5*) was 118% relative to control median and approximately 3 standard deviations above the control median (Fig. 1F). Other identified proteins were outside the control range and >9 standard deviations below control median (Fig. 1F).

Mitochondrial content has previously been calculated in proteomics data using the mean abundance of experimentally validated mitochondrial proteins in the MitoCarta3.0 database [40, 48]. We noticed that the mean abundance of mitochondrial proteins as a group varied between cell lines in our validation cohort (Additional file 2: Fig. S3A) but not control individuals (Additional file 2: Fig. S3B). This phenomenon is typically taken into consideration in enzymology analyses by expressing enzyme rates as citrate synthase (CS) ratios to account for mitochondrial proliferation or cell/tissue variability [15, 49]. CS enzyme activity in our validation cohort varied greatly (Additional file 2: Fig. S3A, upper panel), consistent with altered mitochondrial content. Surprisingly, while CS activity did have a weak positive correlation with the relative abundance of CS protein as detected by proteomics (Additional file 2: Fig. S3C, left panel), it did not correlate with mitochondrial content calculated from the abundance of mitochondrial proteins (Additional file 2: Fig. S3C, middle panel). In line with this, CS protein abundance also did not correlate with mitochondrial content calculated from proteomics data (Additional file 2: Fig. S3C, right panel). Since the nature of proteomics-based RCA is relative

protein abundance, we concluded that mean mitochondrial protein abundance is the appropriate metric to normalise proteomics data. We built a differential mitochondrial abundance correction step into our RCA calculations (see Methods for detailed information). This correction is of benefit for cell lines that may have different mitochondrial content to controls and corrects for mitochondrial content before calculating the relative abundance of each complex.

Proteomics outperforms respiratory chain enzymology in providing functional evidence to mitochondrial disease

We next sought to systematically benchmark our RCA analysis against clinical RCE. RCE was performed on 23 of the 24 fibroblast lines in the validation cohort and was also performed on skeletal muscle (SKM) or lymphoblastoid cell lines (LCLs) for 17 of the 24 patients as a secondary sample type where available. Results are presented relative to CS (Additional file 3: Table S2) and the Bernier criteria [50] were used to classify results. Fibroblast RCE detected a definite defect (<30%, major criteria) in the expected complex(es) for 19 of 24 fibroblast lines (79%) while three [VC4 (*NDUFS2*), VC7 (*NDUFAF1*) and VC10 (*NDUFB10*)] had a probable defect (minor criteria) and RCE did not detect a defect in VC19 (*COX6B1*) fibroblasts (Fig. 2A left panel, Additional file 3: Table S2). When skeletal muscle or LCLs were also available, RCE revealed a major defect in 9 of 17 of the analyses (53%) and a minor defect in four (23%) while three were not deficient (18%) and one was not available (6%) (Fig. 2A, right panel).

Relative complex abundance (RCA) analysis was performed incorporating the correction for mitochondrial content (Additional file 2: Fig. S4) as described above. We classified a major defect as an RCA abundance $\leq 65\%$ relative to controls or $\leq 75\%$ with absent detection of the protein of interest in the proband with >2 peptides detected in controls while minor defects were classified by an RCA abundance of $\leq 75\%$ relative to controls (Additional file 3: Table S2). Using these criteria, a major RCA defect was detected in 83% of the cell lines in the validation cohort, a minor defect in a single case, VC19 (*COX6B1*), and no defect was detected in three cell lines with mtDNA variants (Fig. 2B). Overall, there is no strong correlation between RCE activity and an RCA value relative to control ($R=0.072$, $p=0.78$) (Fig. 2C).

For isolated complex I disorders, 83% (10/12 patients) had a complex I abundance lower than 75% relative to controls analysed ($p<0.0001$). Two of the three complex I-deficient fibroblast lines harbouring missense mtDNA-encoded variants were refractory to RCA analysis but diagnostic by RCE. mtDNA variant heteroplasmy in fibroblasts was 92% for VC6 (*MT-ND1*) and

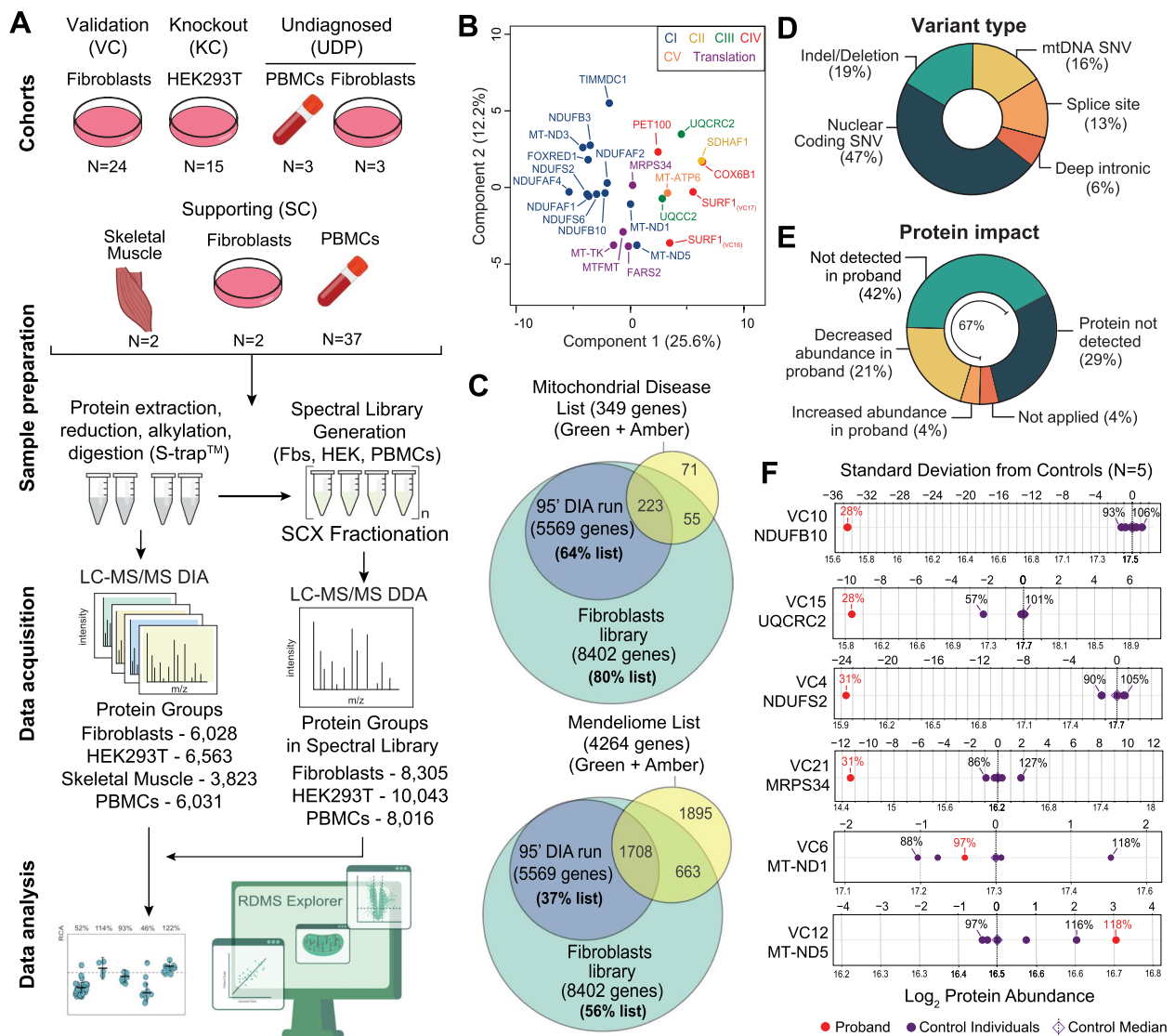


Fig. 1 Study design and validation cohort analysis. **A** Quantitative proteomics experimental design overview. A fibroblast validation cohort (VC), HEK293T knockout cohort (KC), undiagnosed patient cohort (UDP) and supporting cohort (SC) prepared using S-Trap™ columns. Digested peptides were subjected to liquid chromatography tandem mass spectrometry (LC-MS/MS) data-independent acquisition (DIA). Pooled control peptides were fractionated using strong cation exchange (SCX) chromatography and data acquired as data-dependent acquisition (DDA) to generate spectral libraries for fibroblasts (Fbs), HEK293T (HEK) and PBMCs. Raw data were searched using Spectronaut® software and data analyses were performed with a combination of Perseus software, Python and R. **B** Principal component analysis (PCA) of the fibroblast validation cohort (N=24) relative to controls based on the differential abundance of whole cell proteins calculated from a two-sided *t*-test. **C** Venn diagram showing the coverage of Mitochondrial disease (v. 0.787, top panel) and Mendeliome (v. 0.12869, bottom panel) lists including green (diagnostic-grade) and amber (borderline diagnostic-grade) genes retrieved from PanelApp Australia [44]. **D** Summary of the genetic variant types analysed in the validation cohort (VC). **E** Summary of the findings in the VC based on protein identification and abundance. In 42% (10/24) of the cases, the protein expected to be affected by the genetic variant is not detected in the patient while it is detected in the controls. In 29% (7/24) of the cases, the protein is not detected via quantitative proteomics, in 21% (5/24) of the cases, the protein is decreased in abundance in the patient compared to the 5 controls, and in 4% (1/24) of the cases, the protein is increased compared to the controls analysed. SNV=single nucleotide variant. **F** Protein standard deviation from control median of the respective affected gene in controls (purple) and probands (red) in the validation cohort (VC). Standard deviation was calculated from the median control variance

71% for VC12 (*MT-ND5*), highlighting a limitation of our approach in the detection of some mtDNA-driven disorders. Importantly, in all 10 fibroblast lines where RCA

was diagnostic for a complex I disorder, lower abundance (<65% relative to controls) of complexes III, IV and V was not noted (Additional file 2: Fig. S4). While complex II

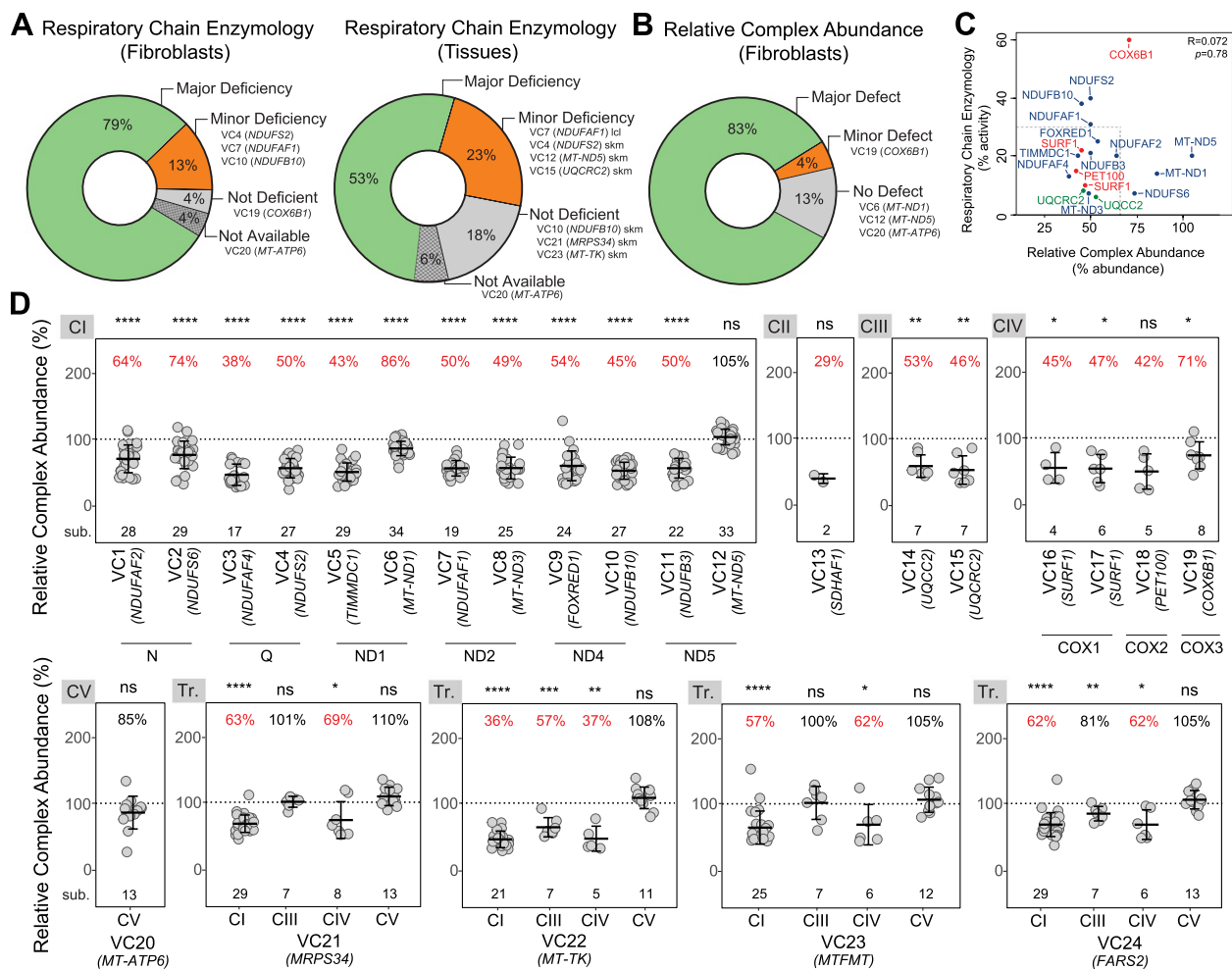


Fig. 2 Proteomics outperforms clinical respiratory chain enzymology in detection of mitochondrial disorders. **A** (left) Summary of the RCE results in fibroblasts according to the Bernier criteria [50]. (right) Summary of the RCE results in tissues (skeletal muscle, SKM or lymphoblastoid cell line, LCL) according to the Bernier criteria [50]. **B** Summary of the RCA results from quantitative proteomic data. **C** Pearson correlation between RCA results and respiratory chain enzymology results for complexes I, III and IV. **D** RCA results of OXPHOS complexes from the validation cohort showing the predicted affected complexes for each cell line. CI–V = complex I–V. Tr. = translation. Middle bar represents mean complex abundance. Upper and lower bars represent 95% confidence interval. Significance was calculated from a two-sided *t*-test between the individual protein means. ****= $p < 0.0001$, ***= $p < 0.001$, **= $p < 0.01$, *= $p < 0.05$, ns = not significant, $p > 0.05$

was reduced to $<75\%$ in four of these, RCE similarly identified a probable complex II defect for one (*FOXRED1*), supporting the accuracy and specificity of RCA analysis. In 7/7 individuals with isolated complex II, III or IV disorders, the abundance of the relevant complex was reduced to $<75\%$ controls (Fig. 2D); however, *t*-test significance varied, especially in CII and IV defects where the number of detected subunits was as low as two. All were specific for the relevant isolated defect except for *UQCRC2* where a complex I abundance of 67% control ($p < 0.0001$) was noted, as expected for complex III disorders [51].

For isolated disorders involving complexes I–IV due to nuclear defects, we determine an RCA value in

fibroblasts of $<65\%$ controls to be diagnostic. The same threshold may also be applied to isolated disorders caused by pathogenic variants in mtDNA including those leading to complex V deficiency; however, smaller reductions may not exclude pathogenicity as seen in VC6 (*MT-ND1*), VC12 (*MT-ND5*) and VC20 (*MT-ATP6*) (Fig. 2D). Interestingly, in the case of VC6 this was likely not due to heteroplasmy, which was 92% NC_012920.1(*MT-ND1*):m.3949C>T in fibroblasts. On the other hand, in VC12 the NC_012920.1(*MT-ND5*):m.13513G>A variant found at 71% in fibroblasts did not show the expected RCA defect while it satisfied the major criteria in RCE (Additional file 3: Table S2), suggesting impaired enzyme kinetics in the absence of a structural complex I defect.

Finally, we found that defects directly impacting mitochondrial translation such as *MRPS34* fibroblasts presenting with a destabilised mitochondrial ribosome small subunit [30], *MT-TK* which encodes the mitochondrial lysine transfer RNA [52], *MTFMT* which encodes the mitochondrial methionyl-tRNA formyltransferase [53], and *FARS2* encoding mitochondrial phenylalanyl-tRNA synthetase, led to an isolated complex I defect or combined complex I and IV defects that each met criteria of an RCA value <65% control (Fig. 2D), consistent with the major criterion observed in RCE (Additional file 3: Table S2). Taken together, fibroblast RCA detected an OXPHOS defect at <65% relative to controls in the expected complex(es) for 20 of 24 fibroblast lines tested (83%) (Fig. 2B). One fibroblast line, VC19 (*COX6B1*), had an RCA of 71% for complex IV relative to controls, which is in line with a previous report showing remaining assembled complex [54] and the peripheral position of the late assembled COX6B1 subunit in the structure of complex IV [55, 56]. Three fibroblast lines where a definitive defect was not observed by RCA harboured variants in mtDNA, suggesting that this class of variant may be more refractory to RCA analysis. Despite this, proteomics-based RCA outperformed RCE in the detection of primary mitochondrial disease. It is important to note here that the nature of proteomics as an untargeted approach means that additional analyses can be performed from the same proteomic data, such as reduced abundance of specific proteins encoded by the gene of interest (Fig. 1E, F) and co-dependent proteins in structural modules (Additional file 2: Fig. S1B). This is exemplified in the VC2 (*NDUFS6*) case where despite showing a complex I abundance of 74%, topographical mapping of complex I subunit abundances against the cryo-EM structure shows specific reduction of the N-module of complex I, providing strong evidence in supporting disease causation.

Application of proteomics in undiagnosed cases with suspected mitochondrial disease

After benchmarking quantitative proteomics and RCA analysis against the validation cohort, we applied our label-free DIA method to six undiagnosed cases where primary fibroblast or PBMCs sample was available for proteomic analysis. A supporting cohort (SC) representing patients with known genetic disorders were used to provide further evidence supporting pathogenicity of variants identified in the undiagnosed cases.

Undiagnosed case 1—UDP1 (*MT-ATP6*)

UDP1 (*MT-ATP6*) was a 4-year-old child who had intra-uterine growth retardation, truncal hypotonia, microcephaly, global developmental delay, left ventricular

noncompaction and Wolff-Parkinson-White syndrome. Biochemically there was a marginal elevation of blood lactate (2.8 mmol/L; RR 0.7–2.0) and 3-methylglutaconic aciduria. Missense variants were identified in *MT-ATP6* [NC_012920.1(*MT-ATP6*):m.8672 T>C;p.(Leu49Pro)], a de novo variant with 81% heteroplasmy in blood, and *ATAD3A* [heterozygous NM_001170535.5:c.683C>T;p.(Thr228Met)] from WES plus mtDNA sequencing from blood and both classified as a VUS. Clinical RCE assays typically do not include complex V activity and proteomics was sought to provide functional evidence. Despite proteomic RCA analysis showing no reduction in abundance of complex V (104% relative to controls), there was a reduction in the number of complex V subunits identified from 13 to 10 compared to the diagnosed *MT-ATP6* patient as well as other cases in the same batch (Fig. 3A and Additional file 2: Fig. S4). The complex V subunits that are not detected in UDP1 (*MT-ATP6*) but are detected in VC20 (*MT-ATP6*) are ATP5IF1, the ATPase inhibitor, and ATP5MD (ATP5MK/DAPIT) and ATP5MPL (ATP5MJ/MP68/6.8PL), which like ATP6, are incorporated at a late stage in the assembly of complex V [55, 57]. The latter suggests a specific turnover of late stage assembled subunits of complex V below the limit of detection of proteomics in the proband, which contributes to the unchanged complex V levels seen in the RCA of UDP1 (*MT-ATP6*). We processed the same data using *q* value sparse run-wise imputation in the Spectronaut® that allows for peptides that were identified in one sample to be imputed at the limit of detection in samples where they were not detected. This allowed us to estimate the fold changes of ATP6 (*MT-ATP6*) and ATP5MPL proteins in UDP1 (*MT-ATP6*) and correlate their reduced levels with VC20 (*MT-ATP6*) as well as confirming unchanged levels of *ATAD3A* (Fig. 3B). To determine if the *ATAD3A* variant p.Thr228Met produces a stable protein, we performed an in silico library-free analysis of the same dataset, but including the *ATAD3A* variant protein sequence. As expected, the peptide containing the methionine at position 228 was only detected in the patient (Fig. 3C), but not controls, and present at ~43% of the abundance relative to the canonical peptide expressed from the other allele (Additional file 2: Fig. S5A). These results indicate that the protein containing the *ATAD3A* p.Met228 is similarly stable as the wild-type protein making it unlikely that a second variant was missed in WES data. Taken together, these results suggest that the *MT-ATP6* p.Leu49Pro variant is the likely diagnosis for this case.

The lack of a complex V defect in proteomics RCA analysis of both *MT-ATP6* cases (VC20 and UDP1) prompted us to analyse additional patients with known pathogenic variants affecting complex V. Supporting cohort probands

SC1 and SC2 were two unrelated infants presenting with lactic acidosis, cardiac abnormalities (persistent patent ductus arteriosus, ventriculo-septal defect and cardiomyopathy), mild dysmorphic facial features, hypospadias, hyperammonaemia and 3-methyl-glutaconic aciduria. Targeted gene sequencing based on this phenotype identified in both individuals a homozygous intronic founder variant NM_017866.6(*TMEM70*):c.317-2A>G classified as class 5/pathogenic, with several patients previously reported [58–62]. Skeletal muscle samples were available for both cases and compared against three unrelated individuals using the library-free DIA approach. Whole muscle proteomic analyses showed reduction of several complex V subunits in SC1 and SC2 respectively (Fig. 3D and E). RCA analyses quantified the relative abundance of complex V at 19% and 20% (Fig. 3F and G), demonstrating that defects in complex V can be detected using RCA analysis. *TMEM70* has also been implicated in complex I assembly [63, 64], although no defects in complex I abundance were noted in these muscle samples.

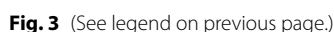
Undiagnosed case 2—UDP4 (*CCDC47*)

UDP4 (*CCDC47*) was born to consanguineous parents, presenting with intrauterine growth restriction, severe failure to thrive, short stature, hypotonia, marked developmental delay, mildly dysmorphic features,

severe pruritus woolly hair, increased plasma bile acids (224 mmol/L; RR<7), Ricketts and decreased mitochondrial CIII activity in liver and muscle [65]. WES performed on DNA extracted from fibroblasts and analysed using a mitochondrial disease gene panel identified single heterozygous missense variants NM_01358921.2(*COQ2*):c.460G>C; p.(Gly154Arg) and NM_020312.4(*COQ9*):c.826C>T p.(Arg276Trp). Suspecting a compound oligogenic mechanism impacting coenzyme Q biosynthesis, RCA analysis was performed on fibroblast cells. No abundance changes to *COQ9* or respiratory chain complexes I–IV were identified, although an abundance of 84% in complex V was noted (Fig. 3H and I). This reduction was regarded as not biologically significant as no rare variants in complex V related genes were flagged from sequencing data. Transcriptomic analysis performed in RNA extracted from skeletal muscle showed a reduced abundance of *CCDC47* transcript (Additional file 2: Fig. S5B). *CCDC47* protein was originally not detected in the proband proteomic data but was well detected in controls (14–18 peptides), supporting the transcriptomic findings. Imputation of proteomics data using a run-wise imputation strategy that estimates the lower limit of the detection of the instrument was used to visualise *CCDC47* protein in the volcano plot (see Methods) (Fig. 3H). Re-analysis of

(See figure on next page.)

Fig. 3 Proteomics supports the diagnosis of patients with suspected mitochondrial disorders. **A** Relative complex abundance (RCA) of complex V subunits in undiagnosed patient UDP1 (*MT-ATP6*) and diagnosed VC20 (*MT-ATP6*) patient. Middle bar represents mean complex abundance. Upper and lower bars represent 95% confidence interval. Significance was calculated from a two-sided *t*-test between the individual protein means. ns = not significant, $p > 0.05$. **B** Correlation between \log_2 fold-changes from whole-cell proteins from run-wise imputed data between undiagnosed patient UDP1 (*MT-ATP6*) and diagnosed patient VC20 (*MT-ATP6*) harbouring mutations in *MT-ATP6* and controls showing reduced abundance in late assembly proteins, *MT-ATP6* and *ATP5MPL*, for both patients. **C** Spectral intensity of the peptide containing the *ATAD3A* p.Thr228Met variant detected in the UDP1 patient but not in controls. **D** Volcano plot of whole cell proteins from SC1 (*TMEM70*) whole-cell skeletal muscle compared to controls ($N = 3$) showing reduced abundance of complex V subunits (orange dots). Vertical lines represent \pm twofold-change equivalent and horizontal lines represent significance p value = 0.05 equivalent from a two-sided *t*-test. **E** Volcano plot of whole cell proteins from SC2 (*TMEM70*) whole-cell skeletal muscle compared to controls ($N = 3$) showing reduced abundance of complex V subunits (orange dots). Vertical lines represent \pm twofold-change equivalent and horizontal lines represent significance p value = 0.05 equivalent from a two-sided *t*-test. **F** Relative complex abundance (RCA) of OXPHOS subunits in undiagnosed patient SC1 (*TMEM70*). Middle bar represents mean complex abundance. Upper and lower bars represent 95% confidence interval. Significance was calculated from a two-sided *t*-test between the individual protein means. **** = $p < 0.0001$, *** = $p < 0.001$, * = $p < 0.05$, ns = not significant, $p > 0.05$. **G** Relative complex abundance (RCA) of OXPHOS subunits in undiagnosed patient SC2 (*TMEM70*). Middle bar represents mean complex abundance. Upper and lower bars represent 95% confidence interval. Significance was calculated from a two-sided *t*-test between the individual protein means. **** = $p < 0.0001$, *** = $p < 0.001$, ** = $p < 0.01$, * = $p < 0.05$. **H** Volcano plot of whole cell proteins using run-wise imputed data from UDP4 (*CCDC47*) fibroblasts compared to controls showing reduced abundance of *CCDC47*. No significant changes to complex V proteins (orange). Vertical lines represent \pm twofold-change equivalent and horizontal lines represent significance p value = 0.05 equivalent from a two-sided *t*-test. **I** Relative complex abundance (RCA) of OXPHOS complexes from UDP4 (*CCDC47*) fibroblasts compared to controls. * = $p < 0.05$, ns = not significant, $p > 0.05$. **J** Volcano plot of whole cell proteins from UDP5 (*NDUFA10*) fibroblasts compared to controls showing reduced abundance of *NDUFA10* and other structural subunits of complex I. Vertical lines represent \pm twofold-change equivalent and horizontal lines represent significance p value = 0.05 equivalent. Blue = complex I subunits. **K** Relative complex abundance (RCA) of OXPHOS complexes from UDP5 (*NDUFA10*) fibroblasts compared to controls ($N = 4$) showing isolated complex I defect. Middle bar represents mean complex abundance. Upper and lower bars represent 95% confidence interval. Significance was calculated from a two-sided *t*-test between the individual protein means. **** = $p < 0.0001$, * = $p < 0.05$, ns = not significant, $p > 0.05$. **L** *NDUFA10* and *HIBCH* protein abundance from two-side *t*-test in SC3, a confirmed *HIBCH* proband, and UDP5 (*NDUFA10*) whole-cell fibroblasts compared to controls, showing an approximate half reduction in *HIBCH* levels in UDP5 (*NDUFA10*, *HIBCH* carrier) compared to SC3 and unchanged *NDUFA10* levels in SC3. **M** Timeline for the rapid proteomics from live fibroblast sample receipt to results for UDP5 (*NDUFA10*) case achieved in less than 5 days



sequencing data identified a homozygous variant NM_020198.3(*CCDC47*):c.431C>G;p.(Thr144Asn). SpliceAI predicted (*d* score 0.964) the activation of a donor-splice site five nucleotides upstream of this variant, and PCR analysis of the muscle cDNA showed the presence of both the missense transcript and a second shorter one, missing 121 bp from the 3' end of exon 4 resulting in a loss-of-function type transcript p.(Val143Glyfs*15) (Additional file 2: Fig. S5C). This variant is not observed in the gnomAD population database nor any clinical cases previously but is predicted to be classified as likely pathogenic/class 4, supported by the observed splicing defect, as well as reduced abundance in *CCDC47* transcript and *CCDC47* protein levels. *CCDC47* has been previously linked to trichohepatoneurodevelopmental syndrome [66] (MIM 618268) which presents an overlapping phenotype to UDP4 (*CCDC47*). The observed reduction in *CCDC47* transcripts due to incorrect splicing is in keeping with previously reported patients, all of whom harbour loss-of-function variants [66, 67].

Undiagnosed case 3—UDP5 (*NDUFA10*)

UDP5 presented with nystagmus, hypotonia, vomiting and weight loss at 20 weeks of age. She had lactic acidosis, concentric left ventricular hypertrophy with 48% ejection fraction, T2 hyperintense lesions in the substantia nigra and passed away at 24 weeks of age. Targeted exome sequencing analysis flagged candidate variants

NM_004544.4(*NDUFA10*):c.914 T>C; p.(Leu305Pro) homozygous VUS/class 3, NM_014362.4(*HIBCH*):c.891+1G>A, heterozygous likely pathogenic/class 4 and NM_018292.5(*QRSL1*):c.22G>C, p.(Glu8Gln) heterozygous VUS/class 3. Fibroblast proteomics detected *NDUFA10* and *HIBCH* below twofold-change (representing >50% reduction) in the patient relative to controls (Fig. 3J and Additional file 2: Fig. S5D). *QRSL1* level was slightly increased but not significant, which led us to further investigate *NDUFA10* and *HIBCH* leads. *NDUFA10* is a structural subunit of complex I and additional functional evidence for pathogenicity could be drawn from reduced abundance of other complex I subunits, with RCA analysis quantifying complex I abundance at 43% in UDP5 (*NDUFA10*) compared to controls, meeting the criteria for a major defect (Fig. 3K). We further assessed whether the levels of *HIBCH* protein were compatible with a carrier (heterozygous) state by analysing fibroblasts from an unrelated patient (SC3) diagnosed with bi-allelic pathogenic variants: NM_014362.4(*HIBCH*):c.891+1G>A and NM_014362.4(*HIBCH*):c.470G>A; p.(Arg157Gln). Proteomic results show that *HIBCH* protein in SC3 (*HIBCH*) is almost two times less abundant than in UDP5 (*NDUFA10*) (Fig. 3L, left panel) while the levels of *NDUFA10* protein were unchanged in SC3 (*HIBCH*), suggesting that a reduction in *NDUFA10* is not a secondary defect from a primary *HIBCH* defect (Fig. 3L right panel). The lack of any decrease in complex

(See figure on next page.)

Fig. 4 Utility of ultra-rapid proteomics supports the diagnosis of critically ill infants with suspected mitochondrial disorders. **A** Venn diagram showing the coverage of Mendeliome genes (PanelApp Australia Green and Amber entries, 4264 genes) in the fibroblast spectral library (55% of Mendeliome list of genes) and PBMC library (52% of Mendeliome list of genes). **B** Principal component analysis (PCA) of the pilot PBMC normative data (*N*=36) for whole-cell proteins (top panel) and MitoCarta3.0 proteins (lower panel). **C** Scatter plot showing the correlation between PBMC (SC4) and fibroblast (SC5) samples based on log₂ fold-changes from whole-cell proteins in a diagnosed patient with variants in *MRPL50* relative to controls [26] showing reduced abundance of the proteins belonging to the large subunits of the mitochondrial ribosome (mtLSU; purple), mtSSU=mitoribosome small subunit (orange). **D** Volcano plot of whole cell proteins from UDP6 (*NDUFA13*) PBMCs compared to controls (*N*=5) showing reduced abundance of *NDUFA13* (orange dot) and other structural subunits of complex I. Vertical lines represent ± twofold-change equivalent and horizontal lines represent significance *p* value = 0.05 equivalent. Blue = complex I subunits. **E** Relative complex abundance (RCA) of OXPHOS complexes from UDP6 (*NDUFA13*) PBMCs compared to controls (*N*=5) showing an isolated complex I defect. Middle bar represents mean complex abundance. Upper and lower bars represent 95% confidence interval. Significance was calculated from a two-sided *t*-test between the individual protein means. ****=*p*<0.0001, *=*p*<0.05, ns=not significant, *p*>0.05. **F** Protein range for *NDUFA13* in PBMCs in UDP6 (*NDUFA13*, red dot) and controls (*N*=5, purple dots) showing standard deviation of −12.2 from the control median. **G** Volcano plot of whole cell proteins from UDP7 (*NDUFAF6*) PBMCs compared to controls (*N*=5) showing reduced abundance of *NDUFS8* and other structural subunits of complex I. Vertical lines represent ± twofold-change equivalent and horizontal lines represent significance *p* value = 0.05 equivalent. Blue = complex I subunits. **H** Relative complex abundance (RCA) of OXPHOS complexes from UDP7 (*NDUFAF6*) PBMCs compared to controls (*N*=5) showing an isolated complex I defect. Middle bar represents mean complex abundance. Upper and lower bars represent 95% confidence interval. Significance was calculated from a two-sided *t*-test between the individual protein means. ****=*p*<0.0001, **=*p*<0.01, ns=not significant, *p*>0.05. **I** Timeline for ultra-rapid proteomics from PBMC sample receipt to results for UDP8 (*NDUFS8*) case achieved in less than 3 business days. **J** Volcano plot of whole cell proteins from UDP8 (*NDUFS8*) PBMCs compared to controls (*N*=5) showing reduced abundance of *NDUFS8* protein (orange dot) and other structural subunits of complex I. Vertical lines represent ± twofold-change equivalent and horizontal lines represent significance *p* value = 0.05 equivalent. Blue = complex I subunits. **K** Relative complex abundance (RCA) of OXPHOS complexes from UDP8 (*NDUFS8*) PBMCs compared to controls (*N*=5) showing isolated complex I defect. Middle bar represents mean complex abundance. Upper and lower bars represent 95% confidence interval. Significance was calculated from a two-sided *t*-test between the individual protein means. ****=*p*<0.0001, **=*p*<0.01, *=*p*<0.05, ns=not significant, *p*>0.05. **L** Protein range for *NDUFS8* in PBMCs in UDP8 (*NDUFS8*, red dot) and controls (*N*=5, purple dots) showing standard deviation of −9.3 from the control median

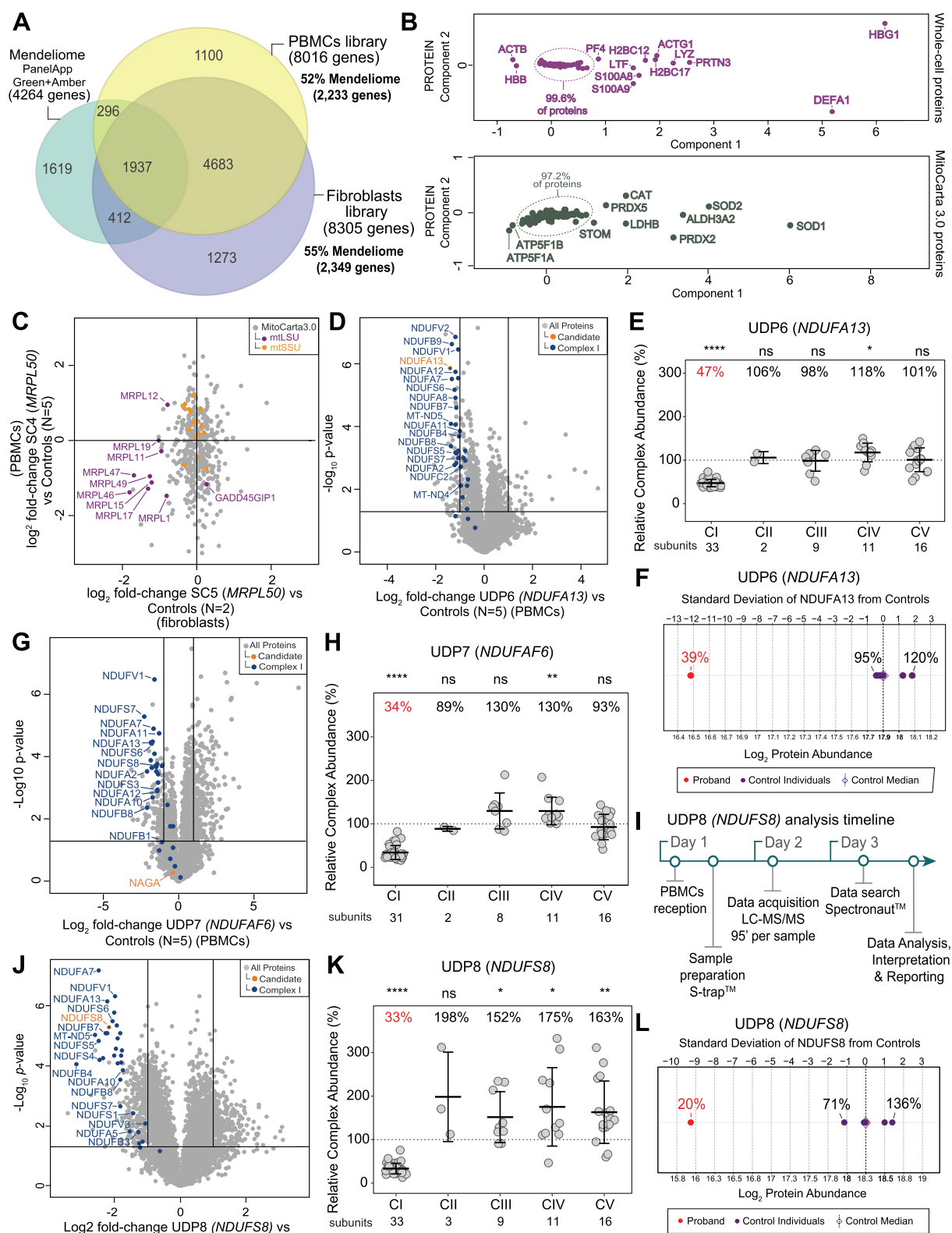


Fig. 4 (See legend on previous page.)

I in SC3 (*HIBCH*) suggests that the phenotype in UDP5 (*NDUFA10*) is likely to have arisen from the *NDUFA10* variant while the *HIBCH* variant is expressed as a carrier and further investigation for a second missed variant in *HIBCH* was not undertaken. UDP5 was the first child of non-consanguineous parents of Māori ethnicity. The mother was 6 weeks pregnant with a second child at the time of analysis and the family sought prenatal genetic testing (PGT). With this in mind, we prioritised sample processing and analysis and were able to return results in less than 4 days from receipt of fibroblasts (Fig. 3M) with the results sufficient to support the upgrade of the *NDUFA10* variant c.914 T>C; p.(Leu305Pro) to likely pathogenic/class 4. This facilitated PGT, which confirmed absence of the *NDUFA10* variant, allowing continuation of the pregnancy and delivery of a healthy child who, at the time of writing, is 15 months old.

Rapid proteomics testing to support variant upgrade using minimally invasive PBMCs

The rapid turnaround time (TAT) in UDP5 (*NDUFA10*) was only possible as fibroblasts from UDP5 were available for analysis at the time of proteomics testing. Establishing and culturing a new fibroblast line typically takes up to ~2 months and requires a skin biopsy [68], which is increasingly considered invasive and can potentially delay a diagnosis. We sought to explore the feasibility of rapid proteomics-based testing for suspected mitochondrial disorders using peripheral blood mononuclear cells (PBMCs), which can be readily obtained from whole blood and have been used in various diagnostic functional testing approaches previously. To test the applicability of PBMCs in proteomic testing, we first generated a fractionated spectral library and compared it against the fibroblast spectral library and coverage of Mendeliome proteins (Fig. 4A). The PBMC library was generated from peptides of 39 normal individuals aged 0–17 years of age and can be used to confidently identify 8,016 gene products, including 52% of known Mendeliome genes [44]. In comparison, our fibroblast spectral library covers 8,305 genes and 55% of the Mendeliome. We performed a principal component analysis (PCA) of whole-cell proteins in PBMC samples from the SC showing that over 99% of the proteins are tightly clustered at the whole-cell level and over 97% at the mitochondrial level (Fig. 4B).

Next, we validated the use of PBMCs against fibroblasts by analysing both sample types from a diagnosed patient with pathogenic variants in *MRPL50* (Twin 2 in [26], SC4 and SC5). *MRPL50* is a structural subunit of the mitoribosome [69] and defects in this subunit lead to impaired assembly of the large mitoribosomal subunit (mtLSU) [26]. We performed a correlation of the log₂ fold-change levels of mitochondrial

proteins identified in both samples relative to controls which showed reduced abundance of multiple proteins belonging to the mtLSU in both sample types (Fig. 4C). RCA quantified the abundance of the mtLSU in 63% and 48% in PBMCs and fibroblasts respectively (Additional file 2: Fig. S5E).

Undiagnosed case 4—UDP6 (*NDUFA13*)

UDP6 (*NDUFA13*) presented at 2 years of age with chronic ataxia. She was the first child to non-consanguineous healthy parents from Iran and had a healthy 2-month-old brother. There was no family history of any neurological issues. She presented with chronic, stable ataxia, having been unsteady and falling frequently since she started walking at 14 months of age. She had mild fine motor delay and a tremor. Her social, language and cognitive development was age appropriate. On examination, UDP6 (*NDUFA13*) had normal growth parameters and was not dysmorphic. She had mild gait ataxia with a broad base. Her tone, power and reflexes were normal in upper and lower limbs bilaterally. Ophthalmology examination was unremarkable. Magnetic resonance imaging (MRI) of brain showed bilateral symmetrical T2/FLAIR hyperintensity of the cerebral peduncles of the midbrain (and possibly the substantia nigra) and two symmetrical foci of high signal in the dorsal medulla with diffusion-weighted imaging (DWI) restriction. There were no basal ganglia or thalamic abnormalities. This was suggestive of a mitochondrial disorder. Serum blood lactate was elevated 2.4 (RR 1.0–1.8). Other metabolic investigations were normal. Audiology assessments and echocardiogram were normal. At 4 years of age, she has ongoing mild ataxia that improved with physiotherapy and was no longer falling. She has recently had deterioration in her vision and been diagnosed with optic neuropathy. Trio exome sequencing identified two in trans heterozygous variants NM_015965.7(*NDUFA13*):c.170G>A; p.(Arg57His) likely pathogenic/class 4 and NM_015965.7(*NDUFA13*):c.187G>A; p.(Glu63Lys) VUS/class 3. Proteomics was sought to provide functional evidence for the VUS/class 3 variant and blood was collected for PBMC isolation as fibroblasts were not available at the time of analysis. Five unrelated PBMCs from age-matched normal donors were used as controls. A volcano plot showed reduction of *NDUFA13* protein and several other complex I subunits in UDP6 (*NDUFA13*) (Fig. 4D) and RCA quantified the isolated complex I defect at 47% control satisfying the criteria for a major defect (Fig. 4E). Analysis of the level of the *NDUFA13* protein in the proband demonstrated a residual abundance of 39%, which corresponds to greater than 12 standard deviations below the control median (Fig. 4F). Proteomics data were

subsequently used as functional evidence to upgrade the NM_015965.7(*NDUFA13*):c.187G>A;p.(Glu63Lys) variant to likely pathogenic/class 4.

Undiagnosed case 5—UDP7 (*NDUFAF6*)

UDP7 (*NDUFAF6*) was referred to the study at 5 months of age with asymmetric early onset growth restriction, central hypotonia, proximal renal tubular dysfunction, macrocytic anaemia, severe exocrine pancreatic insufficiency, liver dysfunction with cholestasis and mild persistent elevated lactate in CSF and blood. MRI showed symmetrical diffusion abnormality involving corticospinal tract, areas of brainstem and medial cerebellar hemisphere. He died at 7 months of age due to progressive bulbar dysfunction with a probable clinical diagnosis of Leigh syndrome. Clinical trio WES identified a single pathogenic (class 5) heterozygous NM_000262.3(*NAGA*):c.973G>A; p.(Glu325Lys) variant, and two in trans variants in *NDUFAF6*, a frameshift NM_152416.4(*NDUFAF6*):c.967delT, p.(Tyr323Ilefs*18) variant and a deep intronic variant, NM_152416.4(*NDUFAF6*):c.298-768 T>C, both classified as VUS/class 3. PBMCs were the sample of choice due to lower invasiveness and potential for fast turnaround. Whole-cell proteomics identified no changes in the abundance of NAGA protein relative to controls (Fig. 4G), suggesting that a missed second variant in trans to NM_000262.3(*NAGA*):c.973G>A; p.(Glu325Lys) is unlikely. *NAGA* encodes the alpha-N-acetylgalactosaminidase, a lysosomal enzyme whose deficiency causes a rare autosomal recessive lysosomal storage disorder. Previous reports of *NAGA*-deficiency show heterogenous presentations ranging from infantile-onset neuroaxonal dystrophy (Schindler disease type I, MIM 609241) to an adult-onset disorder characterised by angiokeratoma corporis diffusum and mild intellectual impairment (Schindler disease type II, also known as Kanzaki disease MIM 609242) [70]. In addition to the proteomic studies, UDP7 (*NDUFAF6*) did not appear to have clinical features consistent with *NAGA*-deficiency, and infants with this condition typically develop normally until about a year old. We then turned our investigations to *NDUFAF6* (*C8orf38*) which encodes an assembly factor involved in biogenesis of the core peripheral arm subunit NDUFS8 of complex I [71] and has previously been associated with the stability of the ND1 module of complex I [72, 73]. Previous reported cases of pathogenic variants in *NDUFAF6* present with a range of symptoms, including Leigh syndrome and the Acadian variant of Fanconi syndrome 5 (proximal renal tubular dysfunction) (FRTS5, MIM 618913) [72–76]. UDP7 (*NDUFAF6*) had clinical features consistent with Leigh syndrome, and while the aetiology of his liver dysfunction and severe exocrine pancreatic insufficiency

was somewhat less clear, both would broadly fit with a mitochondrial cytopathy noting complex I deficiencies often do not correlate perfectly with a single clinical subdivision. The NM_152416.4(*NDUFAF6*):c.298-768 T>C variant has been reported as likely pathogenic previously, specifically in relation to the FRTS5 phenotype [75]. A volcano plot from whole-cell PBMC proteomics data showed reduction in the abundance of several subunits of complex I in UDP7 (*NDUFAF6*), including NDUFS8 (Fig. 4G) with RCA analysis quantifying the isolated complex I defect with a major defect of 34% relative to controls (Fig. 4H). To confirm the impact of the deep intronic *NDUFAF6* variant, cDNA studies performed on fibroblasts showed abnormal splicing at this exon junction including the creation of a cryptic exon besides the canonical transcript (Additional file 2: Fig. S5F). Functional proteomic data, cDNA studies and phenotype match support *NDUFAF6* as being the causative gene for this clinical case, and the VUS/class 3 variants are in the process of re-curation at the time of writing.

Undiagnosed case 6—UDP8 (*NDUFS8*)

UDP8 (*NDUFS8*) was a neonate admitted to hospital presenting with persistent lactic acidemia, hypertrophic cardiomyopathy, left pulmonary artery stenosis, thickened pulmonary valve, hypotonia and microcephaly with progressive deterioration from 4 weeks of age, succumbing at 5 weeks of age. Brain MRI showed abnormalities in the corpus callosum and diffuse increased signal throughout the supratentorial white matter with small foci of gliosis in the peritrigonal regions. Ultra-rapid trio WGS identified a homozygous intronic variant NM_002496.4(*NDUFS8*):c.501+5G>A with biparental inheritance. Due to the critical deteriorating condition, blood was collected from the proband and subjected to ultra-rapid proteomics. Five unrelated age-matched controls were used for comparison and the complete analysis was performed with a 54-h turnaround time (TAT) from PBMC sample reception to the reporting of results to the clinical team (Fig. 4I). Whole-cell proteomic analysis of PBMCs showed significant reduction of several complex I subunits, including NDUFS8 (Fig. 4J) and RCA analysis showed an isolated complex I defect with a major defect of 33% relative to controls (Fig. 4K). Residual abundance of the NDUFS8 protein in the proband was quantified at 20%, representing over 9 standard deviations below the control median (Fig. 4L). Oxford Nanopore long-read sequencing of amplicons generated by PCR from *NDUFS8* cDNA from blood showed skipping of exon 6 (Additional file 2: Fig. S5G) and intron retention between exons 5 and 6 with a premature stop codon (Additional file 2: Fig. S5H), confirming splicing abnormalities arising from the intronic *NDUFS8* variant. The strong phenotype

match together with functional evidence from proteomics and cDNA studies support disease causation due to variants in *NDUFS8* and leading to variant upgrade to likely pathogenic/class 4.

Discussion

The estimated prevalence of rare disease in the population is in the range of 3.5–6%, equivalent to 263–446 million individuals worldwide [77]. There are over 7,000 different rare diseases known, with a current diagnostic yield of ~35–70% from WES or WGS [1–5]. Mitochondrial disease is a group of rare diseases caused by variants in over 300 known genes [11, 21], where RCE has been historically performed to confirm a specific OXPHOS defect in the functional validation of variant pathogenicity [21].

We have previously used an approach we term relative complex abundance (RCA) where proteomics data are used to quantify the residual abundance of OXPHOS complexes in clinical samples from individuals suspected of mitochondrial disease. We have shown that RCA acts as an effective proxy for clinically accredited RCE, including when appropriate samples have not been available [25–27, 29, 30, 78–80]. In an RCA analysis, the abundance of a complex in a sample is calculated from the mean of each individual subunit abundance detected by more than two peptides across each complex. The power of RCA analysis relies on the quantification of multiple peptides per protein in a complex with a high degree of subunit stability co-dependence, as we and others have previously shown for complex I, III, IV, the mitoribosome [16, 22, 25–27, 30, 78, 79, 81, 82] and non-mitochondrial complexes such as the exocyst and nuclear pore complexes [7, 83]. RCE, on the other hand, typically relies on enzyme rate estimates determined in several replicates of patient samples and compared against age-matched controls. In some instances, we have found RCA demonstrated higher sensitivity by detecting a specific OXPHOS defect where RCE was inconclusive [25, 27]. RCA can also show higher specificity for use in functional validation of variant pathogenicity by detecting reduction of specific parts of the complex (e.g. loss of subunits in the catalytic complex I N-module in VC1-*NDUFAF2* and VC2-*NDUFS6*), implicating only the 10 N-module subunits as candidate genes compared with loss of complex I RCE potentially being caused by variants in any of more than 50 genes encoding complex I subunits and assembly factors [35, 84]. In other cases, some variants encoded by the mtDNA resulted in no defect on RCA analysis despite over 70% and 90% heteroplasmy levels in fibroblasts. This suggests that some mtDNA variants can be refractory to RCA analysis, for example, due to a potential enzymatic

and not a structural defect. In these cases, RCE might be a more appropriate test to provide functional evidence. In terms of variant type, mitochondrial DNA variants account for only 0.54% of rare diseases while autosomal recessive variants account for over 41% [85] and are more likely to result in a loss-of-function protein [86], which can be detected via quantitative proteomics. Another unexplored scenario is the utility of proteomic analysis for autosomal dominant mechanisms. However, in cases where the dominant variant could lead to reduction in the protein and/or the abundance of proteins in the impacted complex, as was recently shown in patients with monoallelic defects in *ATP5F1A* and *ATP5MC3* genes [87], RCA proteomics would likely detect defects in complex V. Additional studies are required to provide a better understanding of the utility of proteomics for autosomal dominant disorders.

RCE is typically performed on a tissue biopsy sample (e.g. skeletal muscle, liver) or primary cultured cells (e.g. fibroblasts). Establishing and growing primary fibroblasts from skin biopsies to a sufficient volume of cells for RCE analysis involves weeks to months of cell culture [68], and, in some cases, tissue specificity results in only mild or undetectable defects as measured by RCE [15]. Here we have demonstrated the feasibility of using PBMCs in diagnostic proteomics testing. In our hands, sufficient PBMCs for these analyses can be readily obtained from as little as 1 ml of whole blood and the process from PBMC isolation to data acquisition performed in less than 48 h. Together these properties and the results presented in this study demonstrate that PBMCs can be combined with our ultra-rapid proteomics pipeline for functional validation of variants causing defects in the mitochondrial OXPHOS system and the mitoribosome.

The untargeted nature of quantitative proteomics also allows this technique to be applied beyond mitochondrial disease, as we have shown here for a mitochondrial disease phenocopy (UDP4; *CCDC47*) and elsewhere for nuclear pore, neuronal exocytic vesicle trafficking and rigid spine disorders [7, 83, 88]. Over 50% of known disease-associated genes [44] are routinely detected by our quantitative proteomics pipeline in PBMCs or fibroblasts, and over 45% of all disease genes listed in MIM are part of a protein complex [21]. This means that pathogenic variants in one of these genes can lead to reduction of the protein of interest, which in some cases will result in downstream complex reduction as an additional layer of functional evidence to support variant upgrade. In terms of variant type, we show that quantitative proteomics can provide functional evidence for a wide range of genetic variants including CNV [81], splice site and deep intronic [25, 27], and missense variants [26]. Missense

variants are the most common type of variant accounting for 60% of pathogenic variants associated with autosomal recessive disorders [23] and are usually refractory to transcriptomic analysis. For some cases, proteomics can also provide supportive functional evidence when the protein encoded by the candidate gene is not detectable, either due to protein abundance being below the limit of detection or for genes encoding tRNAs, as seen in VC22 (*MT-TK*), further expanding the potential application of proteomics in rare disease diagnosis.

Conclusions

A genomics-first approach to rare disease diagnosis has markedly increased diagnostic rates and, in the case of rapid and ultra-rapid genomic testing, shortened diagnostic odysseys to days instead of months [7, 89–91]. In the case of mitochondrial and many other rare diseases, diagnoses are often now achieved using just a blood sample, sparing many patients from an invasive biopsy of muscle or other tissues. As a result, diagnostic centres such as ours now receive a third or less of the number of samples for RCE testing than received 10 years ago. This provides an incentive for untargeted functional tests, such as RNA sequencing and proteomics, that could be financially viable and widely available in a pathology-certified context.

This study also highlights the limitations of quantitative proteomics in detecting abundance changes in variants leading to catalytic defects and some mtDNA-encoded variants in fibroblasts. Moreover, the detection of proteins is related to the limit of detection as determined by the liquid chromatography, mass-spectrometry instrumentation and data acquisition methods used. However, recent advances in mass-spectrometry instrumentation including development of the asymmetric track lossless (Astral) analyser offer further improvements in sensitivity and greatly reduced run times [92]. Quantitative proteomics thus offers a further paradigm shift by providing functional evidence for variants in thousands of genes in a single test. This driver will facilitate the translation of proteomics testing for rare diseases into certified pathology laboratories. This is supported by a recent micro-costing study that concludes delivery of proteomics clinically will likely be cost-comparable to pathology-certified respiratory chain enzymology when performed in the Australian context [93]. Moreover, clinically delivered proteomics can potentially replace hundreds of such tests targeted to specific diseases, which are usually restricted to research settings and carry less weight in the upgrade of variants. Our study also demonstrates that proteomics can be delivered alongside ultra-rapid genomic sequencing approaches to provide functional data in a clinically relevant timeline.

Abbreviations

BN-PAGE	Blue native polyacrylamide gel electrophoresis
CI-V	Mitochondrial respiratory chain complexes I–V
CNV	Copy number variant
CS	Citrate synthase
CSF	Cerebrospinal fluid
DDA	Data-dependent acquisition
DIA	Data-independent acquisition
FBs	Fibroblast lines
KC	Knockout cohort (HEK293T)
LC–MS/MS	Liquid chromatography tandem mass spectrometry
LCL	Lymphoblastoid cell line
MIM	Mendelian Inheritance in Men
mtDNAseq	Mitochondrial DNA sequencing
MRI	Magnetic resonance imaging
MRT	Mitochondrial replacement therapy
OXPHOS	Oxidative phosphorylation
PBMCs	Peripheral blood mononuclear cells
PCA	Principal component analysis
PGT	Pre-implantation genetic testing
PND	Prenatal diagnosis
RCE	Respiratory chain enzymology
RCA	Relative complex abundance
RR	Reference range
SC	Supporting cohort
SCX	Strong cation exchange
SDS-PAGE	Sodium dodecyl sulphate–polyacrylamide gel electrophoresis
SKM	Skeletal muscle
TAT	Turnaround time
UDP	Undiagnosed patient
VC	Validation cohort
VUS	Variant of uncertain significance
WES	Whole exome sequencing
WGS	Whole genome sequencing

Supplementary Information

The online version contains supplementary material available at <https://doi.org/10.1186/s13073-025-01467-z>.

Additional file 1: Table S1. Detailed genetic information for the validation (VC), knockout (KC), undiagnosed (UDP) and supporting cohorts (SC).

Additional file 2. Detailed clinical history of VC15 (*UQCRC2*) and VC24 (*FARS2*), Figure S1. Heatmaps and hierarchical clustering of the validation cohort (VC), Figure S2. Protein correlation between cell lines in the validation cohort (VC) and knockout cohort (KC), Figure S3. Mitochondrial abundance, citrate synthase abundance and activity, Figure S4. Relative Complex Abundance (RCA) of OXPHOS complexes in the validation cohort (VC), Figure S5. Orthogonal testing and analysis of undiagnosed cohort and supporting cohort samples.

Additional file 3: Table S2: Relative Complex Abundance (RCA) and Respiratory Chain Enzymology (RCE) results for the validation cohort (VC).

Acknowledgements

We acknowledge and thank all the families who contributed to this study. We thank all members of the Stroud and Stojanovski lab for input into experimental design and interpretation of data. We thank the Bio21 Mass Spectrometry and Proteomics Facility (MMSPF) for the provision of instrumentation, training, and technical support. The Chair in Genomic Medicine awarded to JC is generously supported by The Royal Children's Hospital Foundation. The authors thank staff of the Pathology Collection Department at The Royal Children's Hospital for obtaining the consent of participants and the collection of samples. The authors thank staff of the Anaesthetic and Surgical Departments at the Royal Children's Hospital. MitoMDT Diagnostic Network for Genomics and Omics members include David R. Thorburn, Aleksandra Filipovska, Michael T. Ryan, David A. Stroud, Diana Stojanovski, David Coman, Sean Murray, Ryan L. Davis, John Christodoulou, Roula Ghaoui, Suzanne C. E. H. Sallevelt, Cas Simons, Stefan J. Siira, Shanti Balasubramaniam, Alison G. Compton, Daniel G. MacArthur, Nicole J. Lake,

Amanda Samarasinghe, Yoni Elbaum, Catherine Atthow, Pauline McGrath, Ellenore M Martin, Madeleine Harris, Tegan Stait, Leah E. Frajman, Simone Tregoning.

Authors' contributions

Conceptualization: DHH, DRT, DAS. Methodology: DHH, NJC, LNS, NJL, LuEF, SSCA, TS, ST, LeEF, AMB, DRLR, MB, BoR, AGC, VK, CA. Investigation: DHH, MB, BrR, MJW, AV, CB, HP, JL, ZS, RM, RWT, AGC, WB, NBT, MLF. Visualization: DHH, NJC, LNS, NJL, SSCA. Website design and coding: NJC. Funding acquisition: DHH, JC, AGC, DRT, DAS. Project administration: AS, RB, DRT, DAS. Supervision: PM, ML, RM, RWT, MTR, STC, ZS, JC, AGC, DRT, DAS. Writing – original draft: DHH, DRT, DAS. Writing – review & editing: all authors reviewed and edited the manuscript. All authors read and approved the final manuscript.

Funding

This research was supported by Australian National Health and Medical Research Council (NHMRC) Project and Ideas grants (1140906 to DAS; 1164479 to DRT; 2010939 to MTR), Investigator Fellowships (2009732 to DAS and 2010149 to LuEF) and a Principal Research Fellowship (1155244 to DRT) along with funding by Australian Genomics Health Alliance (Australian Genomics) NHMRC Targeted Call for Research grant GNT1113531. Additional support came from the Australian Medical Research Future Fund Genomics Health Futures Mission (2007959 to DRT, 2016030 to DAS) and Acute Care Genomics (GHFM76747). The US Department of Defense Congressionally Directed Medical Research Programs (PR170396 to DRT). We thank the Mito Foundation for the provision of instrumentation through research equipment grants to DAS and DHH. Additionally, LuEF acknowledges support from the Mito Foundation. This work was also supported by grants from Royal Children's Hospital Foundation [2021–1377]. Work at the MCRI is supported through the Victorian Government's Operational Infrastructure Support Program. RWT is funded by the Wellcome Centre for Mitochondrial Research (203105/Z/16/Z), the Mitochondrial Disease Patient Cohort (UK) (G0800674), the Medical Research Council (MR/W019027/1), the Lily Foundation, Mito Foundation, the Pathological Society, the UK NIHR Biomedical Research Centre for Ageing and Age-related disease award to the Newcastle upon Tyne Foundation Hospitals NHS Trust, LifeArc and the UK NHS Highly Specialised Service for Rare Mitochondrial Disorders of Adults and Children.

Data availability

All the code used to develop the RDMS Explorer website (<https://rdms.app>) and in-house analysis performed in R can be found at (<https://doi.org/10.5281/zenodo.12883602>) and (https://github.com/njcaruana/rdms_oxphos). The mass spectrometry proteomics data have been deposited to the ProteomeXchange Consortium via the PRIDE [94] partner repository with the dataset identifier PXD055473 (<https://www.ebi.ac.uk/pride/archive/projects/PXD055473>). Complete genomic data sets from this study are not able to be released due to patient confidentiality and Institutional Review Board (IRB) approvals. Participants were recruited under a range of IRB approvals. Depending on the specific approval and optional consent chosen by the participant or their parents, specific queries about subsets of genomic data may be able to be provided subject to approval from the Murdoch Children's Research Institute (MCRI) Change Advisory Board. Please contact: david.thorburn@mcri.edu.au. Several online resources were used in preparation of this manuscript. Hierarchical clustering and heatmap plots were generated with Morpheus (<https://software.broadinstitute.org/morpheus/>) [42]. Outlier expression was assessed using the DROP (Detection of RNA Outliers Pipeline) pipeline v0.9.0 (<https://github.com/gagneurlab/drop>) [45]. Venn diagrams were generated with DeepVenn (<https://www.deepvenn.com/>) [43]. Gene lists for green (diagnostic-grade) and amber (borderline diagnostic-grade) for mitochondrial disease (v.0.787) and the Mendeliome (v.0.12869) were retrieved from PanelApp Australia (<https://panelapp-aus.org/>) [44].

Declarations

Ethics approval and consent to participate

This study was conducted in accordance with the revised Declaration of Helsinki and following the Australian National Health and Medical Research Council statement of ethical conduct in research involving humans. Samples were obtained after receiving written, informed consent for diagnostic or research investigations and publication from the respective responsible human ethics

institutional review boards. HREC/RCH/34228, HREC/RCH/34183, HREC/89419/RCHM-2022 and HREC/82160/RCHM-2022 were approved by the Royal Children's Hospital, Melbourne, Ethics in Human Research Committee. HREC/16/MH/251 was approved by the Melbourne Hospital Ethics in Human Research Committee. The REC reference 2002/205 by the Newcastle and North Tyneside Local Research Ethics Committee. Protocol 10/CHW/45 renewed with protocol 2019/ETH11736 (July 2019–March 2025) was approved by Sydney Children's Hospitals Network Human Research Ethics Committee.

Consent for publication

Details from most participants have been published previously as noted in Additional file 1: Table S1. Unless specified below, participants were enrolled into one of a range of Institutional Review Board (IRB) approved study protocols listed in the Ethics approval and consent to participate section, including consent for data sharing and publication. Three of the validation cohort (VC) participants have not been published previously, and the parents of two (VC15, VC24) provided written consent for publication and clinical summaries are provided in Additional file 2. VC13 was lost to follow-up and we are unable to include identifiable data thus clinical details are not included for privacy reasons. If these data are needed for valid clinical reasons, such as variant curation, please contact david.thorburn@mcri.edu.au.

Competing interests

S.T.C. is named inventor of Intellectual Property (IP) related to novel methods to identify splicing variants (WO2020097660A1, WO2020/181333). This IP is owned jointly by The University of Sydney and Sydney Children's Hospitals Network. S.T.C. is Director of Frontier Genomics Pty Australia which has licensed this IP. S.T.C. currently receives no remuneration for this Director role. The remaining authors declare that they have no competing interests.

Author details

¹Department of Biochemistry and Pharmacology, Bio21 Molecular Science and Biotechnology Institute, The University of Melbourne, Melbourne, VIC 3010, Australia. ²Murdoch Children's Research Institute, Melbourne, VIC 3052, Australia. ³Victorian Clinical Genetics Services, Murdoch Children's Research Institute, Melbourne, VIC 3052, Australia. ⁴Institute for Health and Sport (iHeS), Victoria University, Melbourne, VIC 3011, Australia. ⁵Department of Genetics, Yale School of Medicine, New Haven, CT 06510, USA. ⁶Department of Biochemistry and Molecular Biology, Monash Biomedicine Discovery Institute, Monash University, Melbourne 3800, Australia. ⁷Kids Neuroscience Centre, The Children's Hospital at Westmead, Westmead, NSW 2145, Australia. ⁸Children's Medical Research Institute, Westmead, NSW 2145, Australia. ⁹School of Medical Sciences, Faculty of Medicine, University of Sydney, Camperdown, NSW 2006, Australia. ¹⁰Royal Women's Hospital, Melbourne, VIC 3052, Australia. ¹¹Department of Paediatrics, University of Melbourne, Melbourne, VIC 3010, Australia. ¹²Paediatric and Adult National Metabolic Service, Te Toka Tumai, Te Whatu Ora Health New Zealand, Auckland, New Zealand. ¹³Tasmanian Clinical Genetics Service, Tasmanian Health Service, Hobart, TAS 7001, Australia. ¹⁴School of Medicine and Menzies Institute for Medical Research, University of Tasmania, Hobart, TAS 7001, Australia. ¹⁵Department of Metabolic Medicine, Royal Children's Hospital, Melbourne, VIC 3052, Australia. ¹⁶Department of Clinical Genetics, The Canberra Hospital, Canberra, Australian Capital Territory, Australia. ¹⁷Department of Haematology, Royal Children's Hospital, Parkville, VIC, Australia. ¹⁸Kids Cancer Centre, Sydney Children's Hospital, Randwick, NSW, Australia. ¹⁹Department of Molecular and Human Genetics, Baylor College of Medicine, Houston, TX 77030, USA. ²⁰Baylor Genetics, Houston, TX 77021, USA. ²¹Mitochondrial Research Group, Translational and Clinical Research Institute, Faculty of Medical Sciences, Newcastle University, Newcastle Upon Tyne NE2 4HH, UK. ²²NHS Highly Specialised Service for Rare Mitochondrial Disorders, Newcastle Upon Tyne Hospitals NHS Foundation Trust, Newcastle Upon Tyne NE1 4LP, UK.

Received: 18 September 2024 Accepted: 2 April 2025

Published online: 22 May 2025

References

1. Haack TB, Haberberger B, Frisch EM, Wieland T, Iuso A, Gorza M, et al. Molecular diagnosis in mitochondrial complex I deficiency using exome sequencing. *J Med Genet*. 2012;49(4):277–83.

2. Taylor RW, Pyle A, Griffin H, Blakely EL, Duff J, He L, et al. Use of whole-exome sequencing to determine the genetic basis of multiple mitochondrial respiratory chain complex deficiencies. *JAMA*. 2014;312(1):68–77.
3. Ohtake A, Murayama K, Mori M, Harashima H, Yamazaki T, Tamaru S, et al. Diagnosis and molecular basis of mitochondrial respiratory chain disorders: exome sequencing for disease gene identification. *Biochim Biophys Acta*. 2014;1840(4):1355–9.
4. Wortmann SB, Koolen DA, Smeitink JA, van den Heuvel L, Rodenburg RJ. Whole exome sequencing of suspected mitochondrial patients in clinical practice. *J Inher Metab Dis*. 2015;38(3):437–43.
5. Davis RL, Kumar KR, Puttick C, Liang C, Ahmad KE, Edema-Hildebrand F, et al. Use of whole-genome sequencing for mitochondrial disease diagnosis. *Neurology*. 2022;99(7):e730–42.
6. Chung CCY, Leung GKC, Mak CCY, Fung JLF, Lee M, Pei SLC, et al. Rapid whole-exome sequencing facilitates precision medicine in paediatric rare disease patients and reduces healthcare costs. *Lancet Reg Health West Pac*. 2020;1:100001.
7. Lunke S, Bouffler SE, Patel CV, Sandaradura SA, Wilson M, Pinner J, et al. Integrated multi-omics for rapid rare disease diagnosis on a national scale. *Nat Med*. 2023;29(7):1681–91.
8. Nurchis MC, Altamura G, Riccardi MT, Radio FC, Chillemi G, Bertini ES, et al. Whole genome sequencing diagnostic yield for paediatric patients with suspected genetic disorders: systematic review, meta-analysis, and GRADE assessment. *Arch Public Health*. 2023;81(1):93.
9. Wright CF, Campbell P, Eberhardt RY, Aitken S, Perrett D, Brent S, et al. Genomic diagnosis of rare pediatric disease in the United Kingdom and Ireland. *N Engl J Med*. 2023;388(17):1559–71.
10. Richards CS, Bale S, Bellissimo DB, Das S, Grody WW, Hegde MR, et al. ACMG recommendations for standards for interpretation and reporting of sequence variations: revisions 2007. *Genet Med*. 2008;10(4):294–300.
11. Frazier AE, Thorburn DR, Compton AG. Mitochondrial energy generation disorders: genes, mechanisms, and clues to pathology. *J Biol Chem*. 2019;294(14):5386–95.
12. Gorman GS, Chinnery PF, DiMauro S, Hirano M, Koga Y, McFarland R, et al. Mitochondrial diseases. *Nat Rev Dis Primers*. 2016;2:16080.
13. Skladal D, Halliday J, Thorburn DR. Minimum birth prevalence of mitochondrial respiratory chain disorders in children. *Brain*. 2003;126(Pt 8):1905–12.
14. Smeets HJM, Sallevelt S, Herbert M. Reproductive options in mitochondrial disease. *Handb Clin Neurol*. 2023;194:207–28.
15. Frazier AE, Vincent AE, Turnbull DM, Thorburn DR, Taylor RW. Assessment of mitochondrial respiratory chain enzymes in cells and tissues. *Methods Cell Biol*. 2020;155:121–56.
16. Kremer LS, Bader DM, Mertes C, Kopajtich R, Pichler G, Iuso A, et al. Genetic diagnosis of Mendelian disorders via RNA sequencing. *Nat Commun*. 2017;8:15824.
17. Yezpe VA, Gusic M, Kopajtich R, Mertes C, Smith NH, Alston CL, et al. Clinical implementation of RNA sequencing for Mendelian disease diagnostics. *Genome Med*. 2022;14(1):38.
18. Fresard L, Smail C, Ferraro NM, Teran NA, Li X, Smith KS, et al. Identification of rare-disease genes using blood transcriptome sequencing and large control cohorts. *Nat Med*. 2019;25(6):911–9.
19. Murdock DR, Dai H, Burrage LC, Rosenfeld JA, Ketkar S, Muller MF, et al. Transcriptome-directed analysis for Mendelian disease diagnosis overcomes limitations of conventional genomic testing. *J Clin Invest*. 2021;131(1):e141500.
20. Chen E, Facio FM, Aradhya KW, Rojahn S, Hatchell KE, Aguilar S, et al. Rates and classification of variants of uncertain significance in hereditary disease genetic testing. *JAMA Netw Open*. 2023;6(10):e2339571.
21. Alston CL, Stenton SL, Hudson G, Prokisch H, Taylor RW. The genetics of mitochondrial disease: dissecting mitochondrial pathology using multi-omic pipelines. *J Pathol*. 2021;254(4):430–42.
22. Kopajtich R, Smirnov D, Stenton SL, Loipfinger S, Meng C, Scheller IF, et al. Integration of proteomics with genomics and transcriptomics increases the diagnostic rate of Mendelian disorders. *medRxiv*. 2021:2021.03.09.21253187.
23. Xiao Q, Lauschkne VM. The prevalence, genetic complexity and population-specific founder effects of human autosomal recessive disorders. *NPJ Genom Med*. 2021;6(1):41.
24. Sahni N, Yi S, Taipale M, Fuxman Bass JL, Coulombe-Huntington J, Yang F, et al. Widespread macromolecular interaction perturbations in human genetic disorders. *Cell*. 2015;161(3):647–60.
25. Amarasekera SSC, Hock DH, Lake NJ, Calvo SE, Gronborg SW, Krzesinski EI, et al. Multi-omics identifies large mitoribosomal subunit instability caused by pathogenic MRPL39 variants as a cause of pediatric onset mitochondrial disease. *Hum Mol Genet*. 2023;32(15):2441–54.
26. Bakhshalizadeh S, Hock DH, Siddall NA, Kline BL, Sreenivasan R, Bell KM, et al. Deficiency of the mitochondrial ribosomal subunit, MRPL50, causes autosomal recessive syndromic premature ovarian insufficiency. *Hum Genet*. 2023;142(7):879–907.
27. Helman G, Compton AG, Hock DH, Walkiewicz M, Brett GR, Pais L, et al. Multiomic analysis elucidates complex I deficiency caused by a deep intronic variant in NDUFB10. *Hum Mutat*. 2021;42(1):19–24.
28. Horvath R, Scharfe C, Hoeltzenbein M, Do BH, Schroder C, Warzok R, et al. Childhood onset mitochondrial myopathy and lactic acidosis caused by a stop mutation in the mitochondrial cytochrome c oxidase III gene. *J Med Genet*. 2002;39(11):812–6.
29. Van Haute L, O'Connor E, Diaz-Maldonado H, Munro B, Polavarapu K, Hock DH, et al. TEFM variants impair mitochondrial transcription causing childhood-onset neurological disease. *Nat Commun*. 2023;14(1):1009.
30. Lake NJ, Webb BD, Stroud DA, Richman TR, Ruzzenente B, Compton AG, et al. Biallelic mutations in MRPS34 lead to instability of the small mitoribosomal subunit and Leigh syndrome. *Am J Hum Genet*. 2017;101(2):239–54.
31. Rius R, Compton AG, Baker NL, Balasubramaniam S, Best S, Bhattacharya K, et al. The Australian Genomics Mitochondrial Flagship: a national program delivering mitochondrial diagnoses. *Genet Med*. 2024;27:101271.
32. Hoq M, Karlaftis V, Mathews S, Burgess J, Donath SM, Carlin J, et al. A prospective, cross-sectional study to establish age-specific reference intervals for neonates and children in the setting of clinical biochemistry, immunology and haematology: the HAPPI Kids study protocol. *BMJ Open*. 2019;9(4):e025897.
33. Yang Y, Muzny DM, Reid JG, Bainbridge MN, Willis A, Ward PA, et al. Clinical whole-exome sequencing for the diagnosis of Mendelian disorders. *N Engl J Med*. 2013;369(16):1502–11.
34. Akesson LS, Eggers S, Love CJ, Chong B, Krzesinski EI, Brown NJ, et al. Early diagnosis of Pearson syndrome in neonatal intensive care following rapid mitochondrial genome sequencing in tandem with exome sequencing. *Eur J Hum Genet*. 2019;27(12):1821–6.
35. Stroud DA, Surgenor EE, Formosa LE, Reljic B, Frazier AE, Dibley MG, et al. Accessory subunits are integral for assembly and function of human mitochondrial complex I. *Nature*. 2016;538(7623):123–6.
36. Ran FA, Hsu PD, Wright J, Agarwala V, Scott DA, Zhang F. Genome engineering using the CRISPR-Cas9 system. *Nat Protoc*. 2013;8(11):2281–308.
37. Robinson DRL, Hock DH, Muellner-Wong L, Kugapreethan R, Reljic B, Surgenor EE, et al. Applying sodium carbonate extraction mass spectrometry to investigate defects in the mitochondrial respiratory chain. *Front Cell Dev Biol*. 2022;10:786268.
38. Kulak NA, Pichler G, Paron I, Nagaraj N, Mann M. Minimal, encapsulated proteomic-sample processing applied to copy-number estimation in eukaryotic cells. *Nat Methods*. 2014;11(3):319–24.
39. Bruderer R, Bernhardt OM, Gandhi T, Miladinovic SM, Cheng LY, Messner S, et al. Extending the limits of quantitative proteome profiling with data-independent acquisition and application to acetaminophen-treated three-dimensional liver microtissues. *Mol Cell Proteomics*. 2015;14(5):1400–10.
40. Rath S, Sharma R, Gupta R, Ast T, Chan C, Durham TJ, et al. MitoCarta3.0: an updated mitochondrial proteome now with sub-organellar localization and pathway annotations. *Nucleic Acids Res*. 2021;49(D1):D1541–7.
41. Tyanova S, Cox J. Perseus: a bioinformatics platform for integrative analysis of proteomics data in cancer research. *Methods Mol Biol*. 2018;1711:133–48.
42. Morpheus: versatile matrix visualization and analysis software: Broad Institute. Available from: <https://software.broadinstitute.org/morpheus/>.
43. Hulsen T. DeepVenn -- a web application for the creation of area-proportional Venn diagrams using the deep learning framework Tensorflow. js2022 September 01, 2022. arXiv:2210.04597p. Available from: <https://ui.adsabs.harvard.edu/abs/2022arXiv221004597H>.

44. Martin AR, Williams E, Foulger RE, Leigh S, Daugherty LC, Niblock O, et al. PanelApp crowdsources expert knowledge to establish consensus diagnostic gene panels. *Nat Genet.* 2019;51(11):1560–5.
45. Yezep VA, Mertes C, Muller MF, Klaproth-Andrade D, Wachutka L, Fresard L, et al. Detection of aberrant gene expression events in RNA sequencing data. *Nat Protoc.* 2021;16(2):1276–96.
46. Calvo SE, Compton AG, Hershman SG, Lim SC, Lieber DS, Tucker EJ, et al. Molecular diagnosis of infantile mitochondrial disease with targeted next-generation sequencing. *Sci Transl Med.* 2012;4(118):118ra10.
47. Li H. Minimap2: pairwise alignment for nucleotide sequences. *Bioinformatics.* 2018;34(18):3094–100.
48. Granata C, Caruana NJ, Botella J, Jamnick NA, Huynh K, Kuang J, et al. High-intensity training induces non-stoichiometric changes in the mitochondrial proteome of human skeletal muscle without reorganisation of respiratory chain content. *Nat Commun.* 2021;12(1):7056.
49. Thompson K, Stroud DA, Thorburn DR, Taylor RW. Investigation of oxidative phosphorylation activity and complex composition in mitochondrial disease. *Handb Clin Neurol.* 2023;194:127–39.
50. Bernier FP, Boneh A, Dennett X, Chow CW, Cleary MA, Thorburn DR. Diagnostic criteria for respiratory chain disorders in adults and children. *Neurology.* 2002;59(9):1406–11.
51. Acin-Perez R, Bayona-Bafaluy MP, Fernandez-Silva P, Moreno-Loshuertos R, Perez-Martos A, Bruno C, et al. Respiratory complex III is required to maintain complex I in mammalian mitochondria. *Mol Cell.* 2004;13(6):805–15.
52. Rahman S, Blok RB, Dahl HH, Danks DM, Kirby DM, Chow CW, et al. Leigh syndrome: clinical features and biochemical and DNA abnormalities. *Ann Neurol.* 1996;39(3):343–51.
53. Tucker EJ, Hershman SG, Kohler C, Belcher-Timme CA, Patel J, Goldberger OA, et al. Mutations in MTFMT underlie a human disorder of formylation causing impaired mitochondrial translation. *Cell Metab.* 2011;14(3):428–34.
54. Massa V, Fernandez-Vizarra E, Alshahwan S, Bakhsh E, Goffrini P, Ferrero I, et al. Severe infantile encephalomyopathy caused by a mutation in COX6B1, a nucleus-encoded subunit of cytochrome c oxidase. *Am J Hum Genet.* 2008;82(6):1281–9.
55. Hock DH, Robinson DRL, Stroud DA. Blackout in the powerhouse: clinical phenotypes associated with defects in the assembly of OXPHOS complexes and the mitoribosome. *Biochem J.* 2020;477(21):4085–132.
56. Zong S, Wu M, Gu J, Liu T, Guo R, Yang M. Structure of the intact 14-subunit human cytochrome c oxidase. *Cell Res.* 2018;28(10):1026–34.
57. Signes A, Fernandez-Vizarra E. Assembly of mammalian oxidative phosphorylation complexes I-V and supercomplexes. *Essays Biochem.* 2018;62(3):255–70.
58. Cizkova A, Stranecky V, Mayr JA, Tesarova M, Havlickova V, Paul J, et al. TMEM70 mutations cause isolated ATP synthase deficiency and neonatal mitochondrial encephalocardiomyopathy. *Nat Genet.* 2008;40(11):1288–90.
59. Catteruccia M, Verrigni D, Martinelli D, Torraco A, Agovino T, Bonafe L, et al. Persistent pulmonary arterial hypertension in the newborn (PPHN): a frequent manifestation of TMEM70 defective patients. *Mol Genet Metab.* 2014;111(3):353–9.
60. Torraco A, Verrigni D, Rizza T, Meschini MC, Vazquez-Memije ME, Martinelli D, et al. TMEM70: a mutational hot spot in nuclear ATP synthase deficiency with a pivotal role in complex V biogenesis. *Neurogenetics.* 2012;13(4):375–86.
61. Braczynski AK, Vlaho S, Muller K, Wittig I, Blank AE, Tews DS, et al. ATP synthase deficiency due to TMEM70 mutation leads to ultrastructural mitochondrial degeneration and is amenable to treatment. *Biomed Res Int.* 2015;2015:462592.
62. Magner M, Dvorakova V, Tesarova M, Mazurova S, Hansikova H, Zahorec M, et al. TMEM70 deficiency: long-term outcome of 48 patients. *J Inher Metab Dis.* 2015;38(3):417–26.
63. Sanchez-Caballero L, Elurbe DM, Baertling F, Guerrero-Castillo S, van den Brand M, van Strien J, et al. TMEM70 functions in the assembly of complexes I and V. *Biochim Biophys Acta Bioenerg.* 2020;1861(8):148202.
64. Guerrero-Castillo S, Baertling F, Kownatzki D, Wessels HJ, Arnold S, Brandt U, et al. The assembly pathway of mitochondrial respiratory chain complex I. *Cell Metab.* 2017;25(1):128–39.
65. Mowat D, Kirby DM, Kamath KR, Kan A, Thorburn DR, Christodoulou J. Respiratory chain complex III [correction of complex] in deficiency with pruritus: a novel vitamin responsive clinical feature. *J Pediatr.* 1999;134(3):352–4.
66. Morimoto M, Waller-Evans H, Ammous Z, Song X, Strauss KA, Pehlivan D, et al. Bi-allelic CCDC47 variants cause a disorder characterized by woolly hair, liver dysfunction, dysmorphic features, and global developmental delay. *Am J Hum Genet.* 2018;103(5):794–807.
67. Yang Q, Zhou X, Ling Y, Zhang Q, Yi S, Chen Q, et al. Clinical and genetic analysis of trichohepatoneurodevelopmental syndrome caused by a CCDC47 variant. *Heliyon.* 2024;10(6):e27955.
68. Iannello G, Patel A, Sirabella D, Diaz AG, Hoover BN, Sarmah H, et al. Simple, fast, and efficient method for derivation of dermal fibroblasts from skin biopsies. *Curr Protoc.* 2023;3(3):e714.
69. Amunts A, Brown A, Toots J, Scheres SHW, Ramakrishnan V. Ribosome. The structure of the human mitochondrial ribosome. *Science.* 2015;348(6230):95–8.
70. Bakker HD, de Sonnaville ML, Vreken P, Abeling NG, Groener JE, Keulemans JL, et al. Human alpha-N-acetylgalactosaminidase (alpha-NAGA) deficiency: no association with neuroaxonal dystrophy? *Eur J Hum Genet.* 2001;9(2):91–6.
71. Sung AY, Guerra RM, Steenberge LH, Alston CL, Murayama K, Okazaki Y, et al. Systematic analysis of NDUFAF6 in complex I assembly and mitochondrial disease. *Nat Metab.* 2024;6(6):1128–42.
72. Pagliarini DJ, Calvo SE, Chang B, Sheth SA, Vafai SB, Ong SE, et al. A mitochondrial protein compendium elucidates complex I disease biology. *Cell.* 2008;134(1):112–23.
73. McKenzie M, Tucker EJ, Compton AG, Lazarou M, George C, Thorburn DR, et al. Mutations in the gene encoding C8orf38 block complex I assembly by inhibiting production of the mitochondria-encoded subunit ND1. *J Mol Biol.* 2011;414(3):413–26.
74. Baide-Mairena H, Gaudo P, Marti-Sanchez L, Emperador S, Sanchez-Montanez A, Alonso-Luengo O, et al. Mutations in the mitochondrial complex I assembly factor NDUFAF6 cause isolated bilateral striatal necrosis and progressive dystonia in childhood. *Mol Genet Metab.* 2019;126(3):250–8.
75. Hartmannova H, Piherova L, Tauchmannova K, Kidd K, Acott PD, Crocker JF, et al. Acadian variant of Fanconi syndrome is caused by mitochondrial respiratory chain complex I deficiency due to a non-coding mutation in complex I assembly factor NDUFAF6. *Hum Mol Genet.* 2016;25(18):4062–79.
76. Kim J, Lee J, Jang DH. NDUFAF6-related Leigh syndrome caused by rare pathogenic variants: a case report and the focused review of literature. *Front Pediatr.* 2022;10:812408.
77. Nguengang Wakap S, Lambert DM, Olry A, Rodwell C, Gueydan C, Lanneau V, et al. Estimating cumulative point prevalence of rare diseases: analysis of the Orphanet database. *Eur J Hum Genet.* 2020;28(2):165–73.
78. Van Bergen NJ, Gunanayagam K, Bournazos AM, Walvekar AS, Warmoes MO, Semcesen LN, et al. Severe NAD(P)HX dehydratase (NAXD) neuro-metabolic syndrome may present in adulthood after mild head trauma. *Int J Mol Sci.* 2023;24(4):3582.
79. Tucker EJ, Baker MJ, Hock DH, Warren JT, Jaillard S, Bell KM, et al. Premature ovarian insufficiency in CLPB deficiency: transcriptomic, proteomic and phenotypic insights. *J Clin Endocrinol Metab.* 2022;107(12):3328–40.
80. Van Bergen NJ, Hock DH, Spencer L, Massey S, Stait T, Stark Z, et al. Biallelic variants in PYROXD2 cause a severe infantile metabolic disorder affecting mitochondrial function. *Int J Mol Sci.* 2022;23(2):986.
81. Frazier AE, Compton AG, Kishita Y, Hock DH, Welch AE, Amarasekera SSC, et al. Fatal perinatal mitochondrial cardiac failure caused by recurrent de novo duplications in the ATAD3 locus. *Med (N Y).* 2021;2(1):49–73.
82. Borna NN, Kishita Y, Kohda M, Lim SC, Shimura M, Wu Y, et al. Mitochondrial ribosomal protein PTCD3 mutations cause oxidative phosphorylation defects with Leigh syndrome. *Neurogenetics.* 2019;20(1):9–25.
83. Van Bergen NJ, Ahmed SM, Collins F, Cowley M, Vetro A, Dale RC, et al. Mutations in the exocyst component EXOC2 cause severe defects in human brain development. *J Exp Med.* 2020;217(10):e20192040.
84. Formosa LE, Dibley MG, Stroud DA, Ryan MT. Building a complex complex: assembly of mitochondrial respiratory chain complex I. *Semin Cell Dev Biol.* 2018;76:154–62.
85. Frederiksen SD, Avramovic V, Maroillet T, Lehman A, Arbour L, Tarailo-Graovac M. Rare disorders have many faces: in silico characterization of rare disorder spectrum. *Orphanet J Rare Dis.* 2022;17(1):76.
86. Turner TN, Douville C, Kim D, Stenson PD, Cooper DN, Chakravarti A, et al. Proteins linked to autosomal dominant and autosomal recessive disorders harbor characteristic rare missense mutation distribution patterns. *Hum Mol Genet.* 2015;24(21):5995–6002.

87. Zech M, Kopajtich R, Steinbrucker K, Bris C, Gueguen N, Feichtinger RG, et al. Variants in mitochondrial ATP synthase cause variable neurologic phenotypes. *Ann Neurol*. 2022;91(2):225–37.
88. Dofash LNH, Miles LB, Saito Y, Rivas E, Calcinotto V, Oveissi S, et al. HMGCS1 variants cause rigid spine syndrome amenable to mevalonic acid treatment in an animal model. *Brain*. 2024;awae371. <https://doi.org/10.1093/brain/awae371>.
89. Gorzynski JE, Goenka SD, Shafin K, Jensen TD, Fisk DG, Grove ME, et al. Ultrarapid nanopore genome sequencing in a critical care setting. *N Engl J Med*. 2022;386(7):700–2.
90. Australian Genomics Health Alliance Acute Care F, Lunke S, Eggers S, Wilson M, Patel C, Barnett CP, et al. Feasibility of ultra-rapid exome sequencing in critically ill infants and children with suspected monogenic conditions in the Australian public health care system. *JAMA*. 2020;323(24):2503–11.
91. Dimmock D, Caylor S, Waldman B, Benson W, Ashburner C, Carmichael JL, et al. Project Baby Bear: rapid precision care incorporating rWGS in 5 California children's hospitals demonstrates improved clinical outcomes and reduced costs of care. *Am J Hum Genet*. 2021;108(7):1231–8.
92. Guzman UH, Martinez-Val A, Ye Z, Damoc E, Arrey TN, Pashkova A, et al. Ultra-fast label-free quantification and comprehensive proteome coverage with narrow-window data-independent acquisition. *Nat Biotechnol*. 2024;42(12):1855–66.
93. Santos Gonzalez F, Mordaunt D, Stark Z, Dalziel K, Christodoulou J, Goranitis I. Microcosting diagnostic genomic sequencing: a systematic review. *Genet Med*. 2023;25(6):100829.
94. Perez-Riverol Y, Bai J, Bandla C, Garcia-Seisdedos D, Hewapathirana S, Kamatchinathan S, et al. The PRIDE database resources in 2022: a hub for mass spectrometry-based proteomics evidences. *Nucleic Acids Res*. 2022;50(D1):D543–52.

Publisher's Note

Springer Nature remains neutral with regard to jurisdictional claims in published maps and institutional affiliations.